Relation between Orbital Velocities, Pressure, and Surface Elevation in Nonlinear Nearshore Water Waves

KÉVIN MARTINS,[a] PHILIPPE BONNETON,[a] DAVID LANNES,[b] AND HERVÉ MICHALLET[c]

[a] UMR 5805 EPOC, CNRS, University of Bordeaux, Allée Geoffroy Saint-Hilaire, Pessac, France
[b] UMR 5251 IMB, CNRS, University of Bordeaux, Talence, France
[c] UMR 5519 LEGI, CNRS, University Grenoble Alpes, Grenoble, France

ABSTRACT: The inability of the linear wave dispersion relation to characterize the dispersive properties of nonlinear shoaling and breaking waves in the nearshore has long been recognized. Yet, it remains widely used with linear wave theory to convert between subsurface pressure, wave orbital velocities, and the free surface elevation associated with nonlinear nearshore waves. Here, we present a nonlinear fully dispersive method for reconstructing the free surface elevation from subsurface hydrodynamic measurements. This reconstruction requires knowledge of the dispersive properties of the wave field through the dominant wavenumbers magnitude κ, representative in an energy-averaged sense of a mixed sea state composed of both free and forced components. The present approach is effective starting from intermediate water depths—where nonlinear interactions between triads intensify—up to the surf zone, where most wave components are forced and travel approximately at the speed of nondispersive shallow-water waves. In laboratory conditions, where measurements of κ are available, the nonlinear fully dispersive method successfully reconstructs sea surface energy levels at high frequencies in diverse nonlinear and dispersive conditions. In the field, we investigate the potential of a reconstruction that uses a Boussinesq approximation of κ, since such measurements are generally lacking. Overall, the proposed approach offers great potential for collecting more accurate measurements under storm conditions, both in terms of sea surface energy levels at high frequencies and wave-by-wave statistics (e.g., wave extrema). Through its control on the efficiency of nonlinear energy transfers between triads, the spectral bandwidth is shown to greatly influence nonlinear effects in the transfer functions between subsurface hydrodynamics and the sea surface elevation.

KEYWORDS: Ocean; Gravity waves; Nonlinear dynamics; Waves, oceanic; Data processing/distribution; In situ oceanic observations

1. Introduction

In recent years, remote sensing approaches based on lidar technology (Brodie et al. 2015; Martins et al. 2017b, 2020b) or stereo-video imagery (de Vries et al. 2011; Guimarães et al. 2020) have seen tremendous developments and now allow the collection of accurate and direct measurements of the sea surface elevation in nearshore areas. Yet, subsurface pressure sensors and current velocity meters remain the most robust, easy-to-deploy, and versatile solutions for measuring the transformation of wind-generated waves as they propagate shoreward. The relationship between subsurface wave-induced hydrodynamics and the free surface elevation is, however, not straightforward and has been a subject of research for several decades.

If the pressure field at the sea bottom p is known in both time and space, linear wave theory allows an estimation of the free surface elevation ζ as

$$\hat{\zeta}_{L,s}(\mathbf{k}, t) = K_p(\mathbf{k})\hat{\zeta}_{\mathrm{hyd},s}(\mathbf{k}, t) \tag{1}$$

$$K_p(\mathbf{k}) = \cosh(|\mathbf{k}|h), \tag{2}$$

where $\hat{}$ denotes the spatial Fourier transform, $\mathbf{k}$ is the wavenumber, t is the time variable, K_p refers to the pressure transfer function, and h is the mean water depth. The "s" subscripts used in Eq. (1) for the hydrostatic ($\zeta_{\mathrm{hyd},s}$) and linear ($\zeta_{L,s}$) reconstructions of ζ are intended to highlight the *spatial* character of these reconstructions. The hydrostatic reconstruction $\zeta_{\mathrm{hyd},s}$ is simply related to the spatially varying pressure field p as

$$\zeta_{\mathrm{hyd},s}(X, t) = \frac{p - p_a}{\rho g} - h, \tag{3}$$

where X denotes the two-dimensional spatial coordinate, p_a is the atmospheric pressure, g is the acceleration of gravity, and ρ is the water density. In this context, the linear wave theory also provides a direct relation between the time- and spatially varying orbital wave velocities u at the bottom and $\zeta_{L,s}$:

$$\hat{\zeta}_{L,s}(\mathbf{k}, t) = K_u(\mathbf{k})\hat{u}(\mathbf{k}, t) \tag{4}$$

$$K_u(\mathbf{k}) = \sqrt{\frac{\tanh(|\mathbf{k}|h)}{g|\mathbf{k}|}}\cosh(|\mathbf{k}|h), \tag{5}$$

where K_u refers to the transfer function for orbital wave velocities. In a similar way that p needs to be spatially known in

Eq. (1), Eq. (4) requires knowledge of the spatial evolution of u.

Recently, the first nonlinear fully dispersive reconstruction method for irregular waves was proposed by Bonneton and Lannes (2017):

$$\zeta_{\text{NL},s} = \zeta_{L,s} - \frac{1}{g}\partial_t(\zeta_{L,s}\partial_t\zeta_{L,s}), \tag{6}$$

where ∂_t is the partial time derivative operator and the "NL,s" subscript is used to refer to the nonlinear spatial reconstruction of ζ. Accounting for nonlinearities in the wave field leads to a better reconstruction of ζ, with an accurate description of energy levels at high harmonics (Bonneton and Lannes 2017; Mouragues et al. 2019). Since the linear spatial reconstruction $\zeta_{L,s}$ requires knowledge of the temporal and spatial evolution of p (or u), the application of Eq. (6) in the field is somewhat limited in its current form. However, it is important to note that the formula does not involve any spatial derivative. Thus, it can be used locally (at a fixed position X), provided that an approximation of $\zeta_{L,s}$ is available.

In typical nearshore applications, the pressure is measured at a few locations above the seabed and wavenumber spectra are hardly retrieved from such measurements. The most common approach replaces the spatial Fourier transforms in Eqs. (1) and (4) with temporal ones and uses the linear wave dispersion relation [Eq. (9) below] to link the spatial and temporal information of the wave field. This approach corresponds to the classic transfer function method (TFM; e.g., see Bishop and Donelan 1987) and can be written as follows:

$$\tilde{\zeta}_{L,\kappa_L}(\omega, X) = K_p(\omega)\tilde{\zeta}_{\text{hyd}}(\omega, X) \tag{7}$$

$$K_{p,L}(\omega) = \cosh(\kappa_L h) \tag{8}$$

$$\omega^2 = g\kappa_L \tanh(\kappa_L h), \tag{9}$$

where $\tilde{\ }$ denotes the temporal Fourier transform, $\omega = 2\pi f$ is the angular frequency and κ_L denotes the (single-valued) wavenumber magnitude solution to the linear dispersion equation (κ will, hereafter, denote the wavenumber magnitude). The terms ζ_{L,κ_L} and ζ_{hyd} refer to the linear and hydrostatic *temporal* reconstructions of ζ at a single location X in space, respectively.

Since the TFM relies on the linear dispersion relation, it suffers from its limitations in intermediate and shallow water depths, where nonlinear interactions between triads of frequencies intensify (Phillips 1960; Elgar and Guza 1985a). The nonlinear energy transfers associated with these interactions cause large deviations of dominant wavenumbers κ at high frequencies from theoretical values by the linear dispersion relation (Thornton and Guza 1982; Elgar and Guza 1985b; Herbers et al. 2002; Martins et al. 2021). At a given frequency, these deviations were recently shown to increase with the relative amount of forced energy and the efficiency of nonlinear energy transfers, which is strongly controlled by the spectral bandwidth (Martins et al. 2021). The large overestimation of dominant wavenumbers at high frequencies combined with the exponential growth of $K_{p,L}$ [see Eq. (8)] lead to the blow-up of reconstructed sea surface energy levels in nearshore areas.

Here, it is important to remind that this blow-up only occurs for temporal reconstructions employing the linear dispersion relation [Eq. (9)], and not for linear reconstructions in space (Bonneton and Lannes 2017; Mouragues et al. 2019). A pragmatic solution to this blow-up consists in applying a cutoff frequency. The energy missed in the sea surface spectrum tail with the TFM explains why this approach fails at correctly describing the nonlinear shape and peaky character of nearshore waves. Recent work have reported errors on the significant wave height typically between 5% and 10% near or within the surf zone, while these can reach up to 30% and 60% for individual wave heights and third-order parameters, respectively (Martins et al. 2017a; Bonneton et al. 2018; Mouragues et al. 2019; Martins et al. 2020b). Martins et al. (2021) observed that nonlinear effects on the dispersion relation of irregular waves could be important in water depths characterized by $\mu = (\kappa_p h)^2$ up to 0.5, where κ_p is the peak wavenumber. Thus, nonlinear effects in the transfer functions are also expected much farther seaward of the breaking point. At these depths, nonlinear effects can be better accounted with Eq. (6), however, applying the nonlinear formula to an approximation of $\zeta_{L,s}$ based on the linear dispersion relation (i.e., ζ_{L,κ_L}) is not satisfactory due, in part, to the need for a cutoff frequency to overcome the issues detailed above (Bonneton and Lannes 2017).

Near the breaking point or in the surf zone, most components of the sea surface spectrum associated with a typical incident swell propagate approximately at the speed of nondispersive shallow-water waves (Thornton and Guza 1982; Elgar and Guza 1985b; Herbers et al. 2002; Martins et al. 2021). For such shallow water depths, Bonneton et al. (2018) proposed a nonlinear weakly dispersive reconstruction method, which works in the temporal domain and has the advantage of not requiring prior knowledge of $\kappa(\omega)$. Furthermore, the reconstruction has the benefit of not requiring a cutoff frequency, except for preventing noise overamplification at high frequencies. The linear (SL) and nonlinear (SNL) weakly dispersive formula derived by Bonneton et al. (2018) read

$$\zeta_{\text{SL}} = \zeta_{\text{hyd}} - \frac{h}{2g}\partial_t^2\zeta_{\text{hyd}}, \tag{10}$$

$$\zeta_{\text{SNL}} = \zeta_{\text{SL}} - \frac{1}{g}\partial_t(\zeta_{\text{SL}}\partial_t\zeta_{\text{SL}}). \tag{11}$$

The nonlinear formula [Eq. (11)] was shown to accurately describe the sea surface energy levels at high harmonics both outside (Bonneton et al. 2018; Mouragues et al. 2019) and in the surf zone (Martins et al. 2020a,b). The correct description of the sea surface spectrum tail leads to more accurate estimates of high-order wave shape parameters (e.g., the wave skewness) and wave-by-wave statistics (including wave extrema). The weakly dispersive approach performs best in the shallow water limit, where all wave components travel at the speed of nondispersive shallow-water waves. This occurs principally around the mean breaking location and in the surf zone. For narrow-banded swell incident wave conditions, good performances of the weakly dispersive formula are also expected much farther seaward in the shoaling zone [μ up to 0.2 in Mouragues et al. (2019), $\mu \sim 0.24$ in this study].

Even when the most energetic components of a typical incident wave field enter shallow waters ($\mu \lesssim 0.3$), free components can still dominate over forced ones in the high-frequency part of the spectrum. This is expected to occur for μ typically between 0.15 and 0.3, in the presence of relatively strong wind seas or for wave conditions characterized by broad or bimodal spectra. In such situations, the conditions become too dispersive at high frequencies for the weakly dispersive assumption to remain valid. A more general approach is then required to account for the presence of both free components at high frequencies and intense nonlinear effects in the shoaling region.

The objective of this paper is to propose and assess a nonlinear fully dispersive reconstruction of the free surface elevation from subsurface hydrodynamic measurements (pressure or wave orbital velocities). This nonlinear fully dispersive *temporal* reconstruction is obtained via a local application of Eq. (6) with an approximation for the linear *spatial* reconstruction $\zeta_{L,s}$. This approximation is based on the determination of the dominant wavenumber spectra $\kappa(\omega)$ characterizing the wave field. We show that such information are a key determinant for accurately estimating sea surface energy levels at high frequencies, wherever nonlinear effects are significant. Using the dominant wavenumber spectra $\kappa(\omega)$ allows to accurately quantify the relative contribution—in an energy-averaged sense—of both free and forced components. It also appears critical to correctly quantify both linear and nonlinear effects in the pressure and wave orbital velocities transfer functions for nonlinear nearshore waves.

After describing the theoretical and practical aspects of the different temporal reconstruction methods (section 2), the experimental datasets used herein are briefly presented (section 3). The nonlinear fully dispersive reconstruction is first assessed (section 4) with a laboratory dataset collected at high spatial and temporal resolution [Gently Sloping Beach Experiment (GLOBEX); Ruessink et al. 2013]. This dataset represents an ideal situation, where unidirectional waves are considered and κ spectra can be accurately determined from the highly resolved surface elevation measurements. The present approach is then tested in the field (section 5) for the more challenging case of directionally spread waves (Anglet experiment; Mouragues et al. 2020a). In this case, the reconstructions use an approximation for κ derived from the Boussinesq theory of Herbers et al. (2002), applied either to the hydrostatic or the directly measured surface elevation signal. The results are discussed in section 6, with a particular focus on the role of the spectral bandwidth on nonlinear effects in the transfer functions. Section 7 summarizes the results of this study and provides some perspectives.

2. Theoretical and practical aspects of the reconstruction methods

Prior to describing the reconstruction methods, it is important to note that the approaches based on temporal Fourier transforms suppose that for any frequency ω, $\kappa(\omega)$ is uniquely defined. For the TFM, such a relation is provided by the linear relation dispersion [Eq. (9)], which considers the wave field to be composed by free components only. In the nearshore

region, however, both forced and free components can coexist at a given frequency meaning that energy is spread across different wavenumbers. A dominant wavenumber, representative of this mixed sea state in an energy-averaged sense, thus needs to be used for temporal reconstruction methods. This is a fundamental difference with spatial reconstructions [cf. Eqs (1), (4), and (6)], which directly address the energy repartition across several wavenumbers. If $E(\mathbf{k}, \omega)$—the local wavenumber–frequency energy density spectrum of the stochastic process ζ (i.e., irregular waves)—is known, such a representative wavenumber can be defined through the root-mean-square average wavenumber κ_{rms} (Herbers et al. 2002):

$$\kappa_{rms}(\omega) = \left[\frac{\int_{-\infty}^{\infty}\int_{-\infty}^{\infty} |\mathbf{k}|^2 E(\mathbf{k}, \omega)\, d\mathbf{k}}{\int_{-\infty}^{\infty}\int_{-\infty}^{\infty} E(\mathbf{k}, \omega)\, d\mathbf{k}} \right]^{1/2}. \tag{12}$$

In the following, representative $\kappa(\omega)$ spectra are determined with two different methods. For unidirectional irregular waves propagating in the laboratory (GLOBEX), dominant wavenumber spectra κ_{meas} are estimated directly from cross-spectral analysis between adjacent wave gauges. In practice, we observe that such spectral estimates represent the energy spread across several wavenumbers (see, e.g., appendix A of Martins et al. 2021) and are hence equivalent to κ_{rms} [Eq. (12)]. In the field, κ_{rms} is estimated from the pressure and directly measured surface elevation data collected from single sensors using the Boussinesq theory of Herbers et al. (2002).

a. Linear reconstruction methods

For linear waves, $\kappa(\omega)$ can be determined from the linear wave dispersion relation [Eq. (9), $\kappa = \kappa_L$]. In this case, the transfer function for u measured at δ_m above the seabed reduces to

$$K_{u,L}(\omega) = \frac{\sinh(\kappa_L h)}{\omega \cosh(\kappa_L \delta_m)}, \tag{13}$$

which corresponds to the classic TFM (e.g., see Guza and Thornton 1980), while for the pressure, it simply reads

$$K_{p,L}(\omega) = \frac{\cosh(\kappa_L h)}{\cosh(\kappa_L \delta_m)}. \tag{14}$$

This temporal reconstruction of ζ with the TFM will be denoted with the "L,κ_L" subscript.

The second and third linear temporal methods investigated here use measured (κ_{meas}) or predicted (κ_{rms}) dominant wavenumbers to approximate the spatial reconstruction $\zeta_{L,s}$ in Eq. (6). This is done by directly providing these dominant wavenumbers to either K_p [Eq. (2)] or K_u [Eq. (5)], depending on which hydrodynamic variable is measured, and replace the spatial Fourier transform with a temporal one. This ensures the correct representation of energy spreading across several wavenumbers (e.g., presence of both free and forced components at a particular frequency), and is the key element behind the present fully dispersive reconstruction. The second linear reconstruction, denoted with the "L,κ_{meas}" subscript, only

concerns the laboratory dataset (GLOBEX) for which direct estimates of dominant wavenumbers are available (κ_{meas}). The corresponding reconstruction problem reads:

$$\tilde{\zeta}_{L,\kappa_{\text{meas}}}(\omega, X) = K_u(\omega)\tilde{u}(\omega, X) \qquad (15)$$

$$K_u(\omega) = \sqrt{\frac{\tanh(\kappa_{\text{meas}}h)}{g\kappa_{\text{meas}}}}\frac{\cosh(\kappa_{\text{meas}}h)}{\cosh(\kappa_{\text{meas}}\delta_m)}. \qquad (16)$$

The third linear reconstruction, denoted with the "L,κ_{rms}" subscript, provides the transfer function K_p [Eq. (2)] and K_u [Eq. (5)] with the approximation for κ_{rms} given by Herbers et al. (2002):

$$\kappa_{\text{rms}}(\omega) = \kappa_{\text{sw}}(\omega)\sqrt{1 + \beta_{\text{fr}}(\omega) - \beta_{\text{am}}(\omega)}, \qquad (17)$$

with

$$\kappa_{\text{sw}}(\omega) = \frac{\omega}{\sqrt{gh}}, \qquad (18)$$

$$\beta_{\text{fr}}(\omega) = \frac{h\omega^2}{3g}, \qquad (19)$$

$$\beta_{\text{am}}(\omega) = \frac{3}{2hE(\omega)}\int_{-\infty}^{\infty} \text{Re}\{B(\omega', \omega - \omega')\}\, d\omega', \qquad (20)$$

where $E(\omega)$ and $B(\omega_1, \omega_2)$ are the spectral and bispectral densities of ζ, respectively, and $\text{Re}\{\cdot\}$ denotes the real part. The bispectrum is here defined following Kim and Powers (1979):

$$B(\omega_1, \omega_2) = \mathcal{E}[A(\omega_1)A(\omega_2)A^*(\omega_1 + \omega_2)], \qquad (21)$$

where $A(\omega)$ are the complex Fourier coefficients, * denotes the complex conjugate, and $\mathcal{E}$ is an expected, or ensemble average, value. Equation (17) is based on the evolution equations for the Fourier components of a wave field developed by Herbers and Burton (1997) and was derived assuming that the wave field is weakly nonlinear, weakly dispersive, and that these effects are of similar order (Boussinesq approximation). By introducing the nonlinear parameter $\varepsilon = H_s/2h$, where H_s is the significant wave height, this condition is met for Ursell numbers $\text{Ur} = \varepsilon/\mu \sim O(1)$. Herbers et al. (2002) further assume the water depth to be slowly varying in the direction of propagation, which with our current notation writes $\beta/\sqrt{\mu} \ll 1$, where β is a characteristic bottom slope. For the cases investigated next, this is always fulfilled ($\beta/\sqrt{\mu} = 0.014$–0.2 during GLOBEX; $\beta/\sqrt{\mu} = 0.027$–0.04 in Anglet).

The leading-order term of Eq. (17) (κ_{sw}) represents the wavenumber given by the dispersion relation for nondispersive shallow-water waves [Eq. (18)] while β_{fr} and β_{am} are second-order frequency and amplitude dispersion terms, respectively. If the amplitude dispersion effects are neglected [$\beta_{\text{am}} = 0$ in Eq. (17)], we can also define a linear Boussinesq wavenumber κ_B. Only real values of the bispectrum contribute to amplitude dispersion effects at the order considered in this theory [$O(\mu, \varepsilon)$, see Herbers et al. 2002]. Although the present approach is fully dispersive with κ_{meas} (i.e., no hypothesis required on the wave field dispersive regime), the approximation of κ_{rms} is only weakly dispersive. In the following, the linear reconstruction based on κ_{rms} will hence be described as moderately dispersive, in order to avoid confusions with the weakly dispersive approaches of Bonneton et al. (2018).

b. Weakly nonlinear reconstruction methods

The nonlinear reconstruction formula provided in Eq. (6) is based on a linear *spatial* reconstruction of ζ computed either from the pressure [Eq. (1)] or orbital wave velocities [Eq. (4)] measured at the sea bottom. Bonneton and Lannes (2017) demonstrated that for linear waves, the spatial Fourier transform in these reconstructions can be replaced with the temporal one so that the spatial [Eqs. (1) and (4)] and temporal [Eqs. (7) and (15)] reconstructions are equivalent. This replacement can also be performed in the case of nonlinear waves of permanent forms (all modes propagating at a speed C), as long as $\kappa(\omega/C)$ is used instead of the linear wave dispersion relation (Bonneton and Lannes 2017).

The situation for the more general case of fully dispersive irregular waves propagating in the nearshore is not as straightforward analytically since $\kappa(\omega)$ is not unique. For replacing the spatial Fourier transform with a temporal one in such cases, we here assume that using the dominant wavenumbers κ_{rms} is sufficient to correctly represent the energy spreading across different wavenumbers and pass from a *spatial* to *temporal* reconstruction problem. With the hypothesis that $\zeta_{L,\kappa_{\text{meas}}}$ or $\zeta_{L,\kappa_{\text{rms}}}$ are accurate approximations of $\zeta_{L,s}$ at a given location in space, a local and temporal application of Eq. (6) then becomes possible. The nonlinear reconstruction based on directly measured dominant wavenumbers (subscript "NL,κ_{meas}") or those predicted with Boussinesq theory (subscript "NL,κ_{rms}") are obtained by replacing $\zeta_{L,s}$ in Eq. (6) with the corresponding linear reconstruction, described in the previous section. For the reconstruction that uses directly measured dominant wavenumbers κ_{meas}, this reads:

$$\zeta_{\text{NL},\kappa_{\text{meas}}} = \zeta_{L,\kappa_{\text{meas}}} - \frac{1}{g}\partial_t\left(\zeta_{L,\kappa_{\text{meas}}}\partial_t\zeta_{L,\kappa_{\text{meas}}}\right). \qquad (22)$$

On the right-hand side of Eq. (22), the nonlinear term with temporal derivatives of $\zeta_{L,\kappa_{\text{meas}}}$ represents the contribution from nonlinear interactions to the reconstructed ζ. Note that for the case of p or u measured at an arbitrary height above the seabed, an extra term arises in Eqs. (6) and (22); the reader is referred to Eq. (C4) of Bonneton and Lannes (2017) for the complete formula.

Equation (6) is valid for $\varepsilon\sqrt{\mu} \ll 1$ and hence covers most typical nearshore applications, i.e., from waves of small steepness propagating in intermediate water depths to large-amplitude waves in shallow water depths. Like all the linear reconstructions investigated above, it was derived assuming that the flow is irrotational, meaning that the flow velocity potential is solution to the Laplace equation. The bottom contribution to the nonlinear formula is here neglected, since these terms are negligible over mildly sloping beaches as those considered here (see section 3.4 of Bonneton and Lannes 2017). Over steep slopes, the bottom contribution to the nonlinear formula in the fully dispersive regime remains an open research question. Unlike the linear reconstructions

presented above, the nonlinear correction is locally considered to be one-dimensional. The directional spreading is hence assumed to be small enough so that κ approximates well the magnitude of the wavenumber projected in the main direction of propagation. For large directional spreading angles or crossing seas, nonlinear energy transfers toward high harmonics become slightly less efficient (Herbers and Burton 1997; de Wit et al. 2020). Thus, in such situations, Eqs. (6) and (22) could slightly overestimate the intensity of nonlinear interactions.

In the following, we show that both $\zeta_{\mathrm{NL},\kappa_{\mathrm{meas}}}$ and $\zeta_{\mathrm{NL},\kappa_{\mathrm{rms}}}$ reconstructions successfully reproduce energy levels at high frequencies. In practice, however, a cutoff frequency ω_c in the linear reconstructions $\zeta_{L,\kappa_{\mathrm{meas}}}$ and $\zeta_{L,\kappa_{\mathrm{rms}}}$ is still needed for two distinct reasons. For the fully dispersive approximation $\zeta_{L,\kappa_{\mathrm{meas}}}$, the cutoff is mostly intended for not overamplifying noise in the current/pressure data, which leads to slight or moderate overestimations of energy levels at high frequencies. For the moderately dispersive approximation $\zeta_{L,\kappa_{\mathrm{rms}}}$, it is mostly intended to limit the effects originating from inaccuracies in κ_{rms} spectral estimates at high frequencies. As for the TFM, these inaccuracies at high frequencies potentially lead to a blow-up of sea surface energy levels. Both situations hence have very distinct origins and effects on the reconstructed signal and will be discussed accordingly. The different temporal reconstructions and their associated range of application are recapitulated in Table 1.

3. Experimental datasets

a. GLOBEX

The laboratory dataset was collected during GLOBEX, which was performed in a 110-m-long, 1-m-wide, and 1.2-m-high wave flume located in the Scheldegoot in Delft, the Netherlands (Ruessink et al. 2013). During these experiments, free surface elevation and current velocity data were collected at high spatial and temporal resolution in order to study the transformation of short and infragravity waves propagating over a mildly sloping beach (e.g., see de Bakker et al. 2015; Tissier et al. 2015; Rocha et al. 2017). The high spatial resolution was obtained by repeating each wave test 10 times and moving the wave gauges (sampling at 128 Hz) across the 1:80 concrete beach (see Fig. 1). In addition to wave gauges, five electromagnetic current meters (ECM) were fixed to the movable trolleys and allowed the collection of current velocities at numerous cross-shore locations. An acoustic Doppler velocimeter (ADV) was also deployed at four different locations, as shown in Fig. 1.

This study concentrates on the 70-min-long irregular wave tests of the A series (A1, A2, A3; see Ruessink et al. 2013) during which JONSWAP spectra were imposed at the wave paddle. These wave tests reproduced moderate to energetic sea conditions characterized by broadband to narrowband sea surface spectra; see Table 2. For these experiments, dominant wavenumber κ were computed via cross-spectral analyses of the highly resolved surface elevation dataset (Martins et al. 2021). Besides their relevance for verifying the proposed fully

TABLE 1. Synthesis of the temporal reconstruction methods investigated in this study and their range of application.

Reconstruction of ζ	Type of approach and range of application
$\zeta_{\mathrm{SL}} - \zeta_{\mathrm{SNL}}$	Weakly dispersive approximation of $\zeta_{L,s}$ and $\zeta_{\mathrm{NL},s}$—valid in shallow water only
ζ_{L,κ_L}	Fully dispersive approximation of $\zeta_{L,s}$—valid for linear waves only
$\zeta_{L,\kappa_{\mathrm{rms}}} - \zeta_{\mathrm{NL},\kappa_{\mathrm{rms}}}$	Moderately dispersive approximation of $\zeta_{L,s}$ and $\zeta_{\mathrm{NL},s}$ based on a Boussinesq estimate of κ_{rms}
$\zeta_{L,\kappa_{\mathrm{meas}}} - \zeta_{\mathrm{NL},\kappa_{\mathrm{meas}}}$	Fully dispersive approximation of $\zeta_{L,s}$ and $\zeta_{\mathrm{NL},s}$—valid for $\varepsilon\sqrt{\mu} \ll 1$

dispersive approach, these direct measurements are particularly useful to assess the accuracy of the Boussinesq predictions of κ_{rms} [Eq. (17)] (Herbers et al. 2002) and the corresponding reconstructions. Indeed, in most typical field situations, measurements of dominant wavenumbers κ are not available and Eq. (17) remains the only option to get an estimation of this quantity. For the GLOBEX dataset, bispectra in Eq. (17) were computed on the free surface elevation signals downsampled to 16 Hz by averaging estimates from 126 records of 128 s, which were overlapping by 75%. Statistical stability was increased by merging estimates over three frequencies (e.g., see Elgar and Guza 1985a) yielding approximately 150 equivalent degrees of freedom, and a spectral resolution of 0.023 Hz. The measured and predicted dominant wavenumbers are used in the following to reconstruct the free surface elevation from cross-shore current velocities measured with the ECMs. As the ADV data contained more noise at high frequencies, the data from this sensor was not used for the reconstruction but only to calibrate current velocities as measured by the ECMs (see online supplemental material). Energy spectra of u and ζ were computed by averaging estimates from 63 Hann-windowed records of 128 s, which were overlapping by 50%, yielding approximately 70 equivalent degrees of freedom, and a spectral resolution of 0.008 Hz.

b. Anglet field experiment

In addition to the GLOBEX dataset, we also use data collected in Anglet, France, during field experiments conducted at La Petite Chambre d'Amour beach from 3 to 26 October 2018 (Mouragues et al. 2020a,b). These experiments aimed at studying the wave-induced circulation occurring along this geologically constrained beach under varying incident wave conditions. The data from two particular current profilers are used: SIG1, a Nortek Signature 500 kHz continuously sampling the near-bottom pressure and Eulerian fluid velocities across the vertical at 4 Hz, and SIG2, a Nortek Signature 1000 kHz that sampled similar quantities at 8 Hz. Additionally, both instruments continuously tracked the free surface elevation by acoustic means [acoustic surface tracking (AST)]. The SIG1 and SIG2 pressure sensors were deployed at 0.6 and 0.69 m above the seabed in mean water depths of 13.9 and 8.1 m, respectively. The depth contours around both instruments are nearly parallel to the coastline [see Mouragues et al. (2020a) for further details].
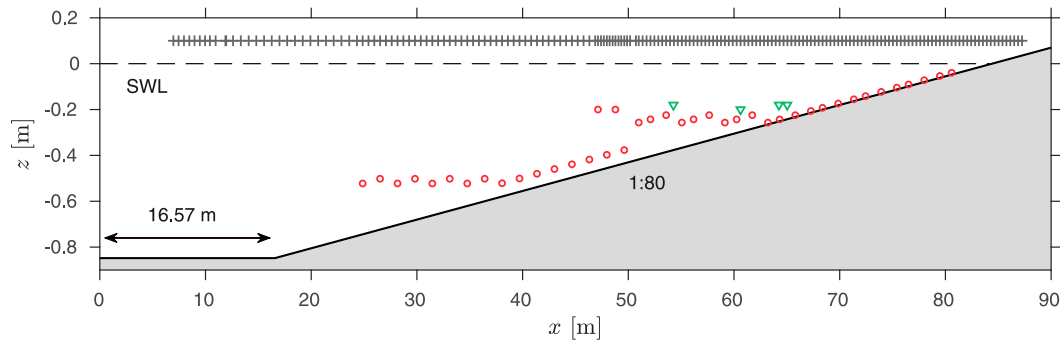
FIG. 1. Elevation z of the 1:80 concrete beach against the cross-shore distance x in the Scheldegoot flume during GLOBEX. The wave paddle is located at $x = 0$ m. The gray "+" symbols show the position of the wave gauges while red circles and green triangles indicate the position of the electromagnetic current meters and acoustic Doppler velocimeters, respectively.

Similar to the GLOBEX experiments, two contrasting events in terms of incident energy and frequency bandwidth were selected among the nearly two weeks during which both instruments collected data simultaneously. Both events consider shoaling waves outside the surf zone so that the measurements from the AST remain fully reliable. The offshore significant wave height H_s and peak wave period T_p measured at the nearest wave buoy [Centre d'Archivage National des Données de Houle In Situ (CANDHIS) buoy 06402, located 3.5 km off the coast in 50-m water depth] were quite similar during both events with $H_s \sim 2$–2.5 m and $T_p \sim 13$ s. Case A (low tide at 0100 local time 15 October 2018) corresponds to a moderate energy event characterized by (frequency) broadband sea surface spectra, while case B (high tide at 1800 local time 13 October 2018) is a relatively more energetic event characterized by narrowband sea surface spectra. The wave directional spreading angle measured offshore was weak during both events, with mean values of 27° and 20° during case A and B, respectively (20° at the energy peak for both events). The offshore mean wave direction was estimated between 290° and 300° W, which corresponds to a mean incident angle smaller than 10° relative to the beach orientation. The temporal mean depth-averaged currents U observed at the two sensors location were <0.1 m s^{-1} during both events which, at the highest frequency of interest here ($5.5f_p = 0.43$ Hz, with f_p the peak wave frequency), corresponds to mean current to (linear) wave phase speed ratio $U/c < 0.03$ at all times. The background mean current is therefore neglected in the present study. Other relevant parameters for these events are given in Table 3.

Dominant κ_{rms} were computed from two different sources: ζ_{hyd} and ζ_{AST}, the free surface directly measured with the AST. Bispectra were computed from 2.2-h-long detrended time series using 61 records of 512 s, which were overlapping by 75%. Stationarity was ensured by selecting ~1.1 h before and after low (case A) or high tide (case B), the maximal water depth variation being only 0.36 m. Energy spectra of ζ were computed by averaging estimates from 61 Hann-windowed records of 512 s, which were overlapping by 75%. Statistical stability was increased by averaging spectral and bispectral estimates over three frequencies yielding approximately 103 and 73 equivalent degrees of freedom, respectively, and a frequency resolution of 0.0059 Hz for both estimates.

4. Assessment of the nonlinear fully dispersive reconstruction methods

In this section, the different reconstruction methods presented in section 3 are assessed using the dataset collected during GLOBEX, for which measurements of $\kappa(\omega)$ are available [denoted $\kappa_{\mathrm{meas}}(\omega)$]. We focus on two of the four regimes of propagation (I–IV) described in Martins et al. (2021): a shoaling situation (stage II) and near-breaking situation (stage III). Besides being of little interest in the present context, the linear regime (stage I) occurs in the deepest section of the flume (up to ~$x = 15$ m) and hence cannot be addressed here since the first current meter was located at $x = 24.86$ m. Similarly, the stage corresponding to

TABLE 2. Significant wave height H_s and discrete peak wave frequency f_p imposed during the three irregular wave tests of GLOBEX. The peak enhancement γ of the JONSWAP spectra characterizes its spectral bandwidth: a value of 3.3 corresponds to broad spectra while a narrowbanded spectra is imposed with $\gamma = 20$.

Test	H_s (m)	f_p (Hz)	γ (—)
A1	0.10	0.633	3.3
A2	0.20	0.444	3.3
A3	0.10	0.444	20

TABLE 3. Relevant parameters for the two events from the Anglet experiments (Mouragues et al. 2020a): significant wave height H_s, peak wave period T_p, mean water depth h, dispersion parameter μ, nonlinearity parameter $\varepsilon = H_s/2h$, and Ursell number Ur $= \varepsilon/\mu$.

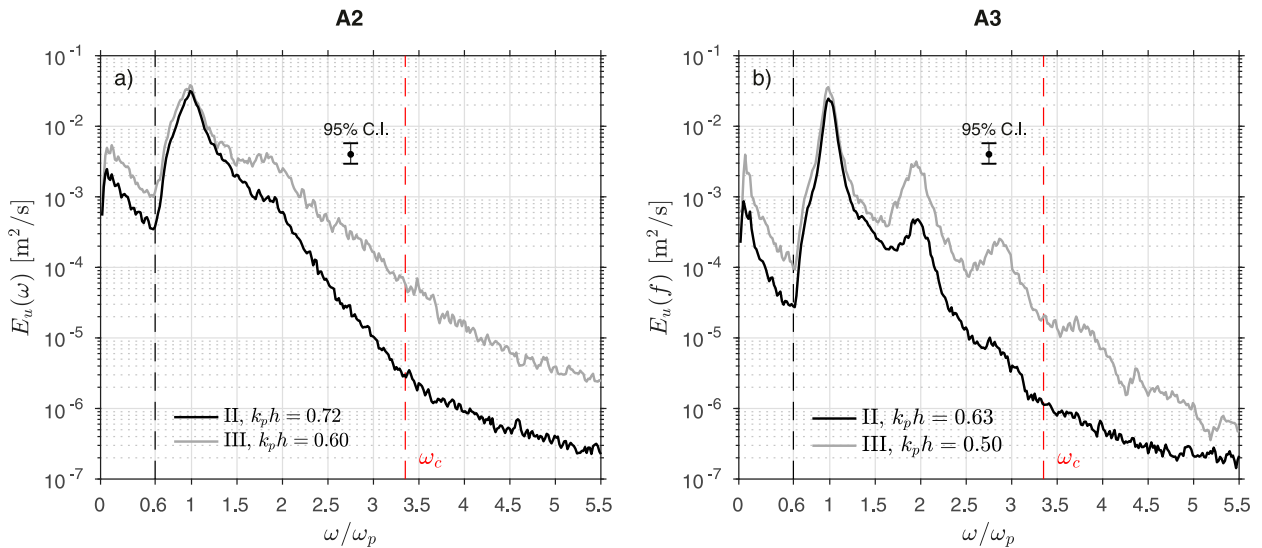| Burst	H_s (m)	T_p (s)	h (m)	μ (—)	ε (—)	Ur
SIG1–case A	2.0	13.0	13.1	0.34	0.08	0.23
SIG1–case B	2.7	13.0	15.3	0.40	0.09	0.22
SIG2–case A	2.2	13.0	7.2	0.18	0.15	0.84
SIG2–case B	3.2	13.0	9.5	0.24	0.17	0.72

FIG. 2. Cross-shore current velocity energy density spectra $E_u(\omega)$ computed at the location in the wave flume corresponding to the stages II (Ur ~ 0.3) and III (Ur ~ 0.7) described in Martins et al. (2021). The frequency axis is normalized by the peak frequency ω_p, which equals 2.79 Hz for both wave test (left) A2 and (right) A3. The value of $k_p h$ for each test and propagation stage is indicated in the legend. The separation between the infragravity and gravity band of frequencies ($0.6\omega_p$) is indicated by the vertical black dashed line. The cutoff frequency ω_c applied to the fully and moderately dispersive linear reconstructions is indicated by the vertical red dashed line.

surf zone conditions (stage IV) is not covered here due to limitations and uncertainties in the measurements collected ~1 cm from the flume bottom, in the vicinity of the boundary layer [see also Aubrey and Trowbridge (1985) for a discussion of ECMs in such conditions]. Nonetheless, the weakly dispersive reconstruction of Bonneton et al. (2018) was already shown to accurately describe both the sea surface energy content at all frequencies and the wave-by-wave characteristics in surf zones (Martins et al. 2020a,b).

The current velocity density spectra $E_u(\omega)$ corresponding to stages II and III are displayed in Fig. 2. The two wave tests compared here (A2 and A3) differ in the energy and spectral bandwidth imposed at the paddle (see also Table 2): A2 corresponds to energetic conditions with broadband spectra while for A3, the conditions are typical of a swell (moderate energy and narrowband spectrum). For both tests, the cutoff frequency for not overamplifying noise in the measurements was determined at $3.35\omega_p$, with ω_p the peak wave angular frequency, based on the slope changes occurring on $E_u(\omega)$ around this frequency.

a. Shoaling of weakly nonlinear waves (II)

During stage II, nonlinear energy transfers between principal components promote the dominance of bound high harmonics in wavenumber spectra (see Figs. 3a,b). The differences in dispersive properties between wave tests A2 and A3 are mainly explained by differences in forced-to-free energy ratio at high harmonics, as estimated in Martins et al. (2021). Although less energetic than for A2, the narrow-banded condition imposed during A3 led to more effective nonlinear energy transfers by sum interactions [$(\omega_p, \omega_p) \rightarrow 2\omega_p$; $(\omega_p, 2\omega_p) \rightarrow 3\omega_p$], so that 70% and 90% of the energy was estimated to be forced around $2\omega_p$ and $3\omega_p$, respectively. These

intense energy transfers explain why measured dominant $\kappa(\omega)$ at high harmonics (e.g., $2\omega_p$, $3\omega_p$, and $4\omega_p$) follow the simple relation $\omega/c(\omega_p)$ (Fig. 3b), suggesting that these components mostly propagate at the same speed as the peak component ω_p. In contrast, during A2, dominant $\kappa(\omega)$ at high frequencies lie between $\omega/c(\omega_p)$ and values predicted by the linear wave dispersion relation (Fig. 3a), which is explained by the weaker amounts of forced energy found during this test (around 20% and 30% at $2\omega_p$ and $3\omega_p$, respectively). The weakly nonlinear approximation of Herbers et al. (2002) [Eq. (17)] provides very accurate estimates of the dominant wavenumbers and describes well its variation across infragravity and gravity frequency bands up to $2.5\omega_p$ for both tests. Components at higher frequencies are too dispersive for Eq. (17) to be accurate and a higher-order theory is probably required. These results are consistent with those from Herbers et al. (2002) who focused on weakly dispersive waves for their comparisons at ω_p, $2\omega_p$, and $3\omega_p$ (data for which $3f_p > 0.25$ Hz were removed for the model assessment).

In such dispersive conditions ($\mu = 0.5$ and 0.4 for A2 and A3, respectively), the large discrepancies of wavenumbers predicted by the linear wave dispersion relation have dramatic effects on the surface elevation signal reconstructed with the TFM at high frequencies (see ζ_{L,κ_L} in Figs. 3c,d). Compared to the direct measurements from the wave gauge (ζ_{wg}), the TFM induces significant overestimation of energy levels starting from $2.5\omega_p$, where in typical applications, a cutoff frequency should be applied. Up to $2.5\omega_p$, this overestimation leads to errors on the significant wave height H_s and mean wave period T_{m02} lower than 2% and 4%, respectively (see appendix for the definition of these bulk parameters), which is considerably lower than those found in the field, for relatively more energetic and directionally broad
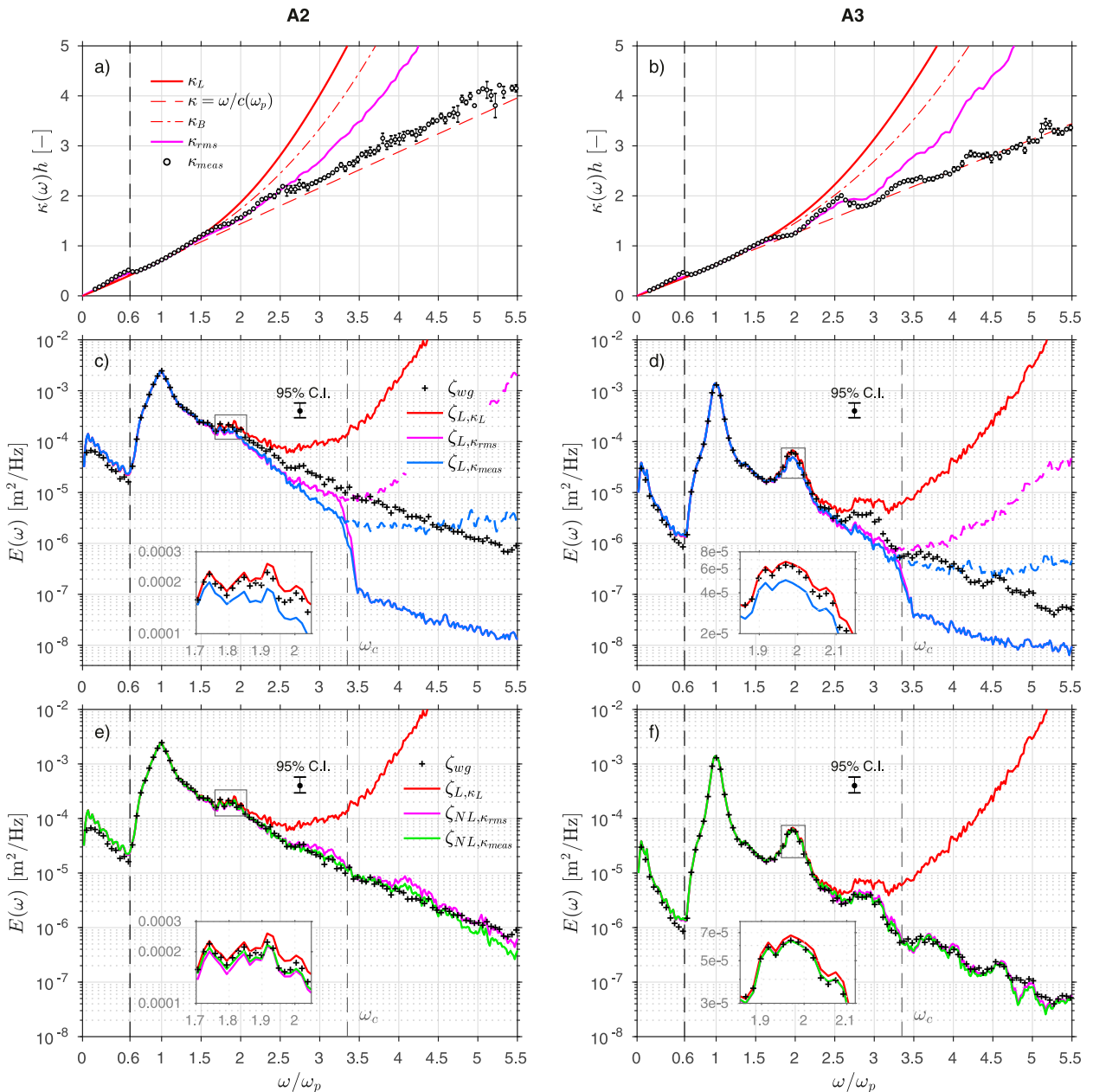
FIG. 3. (a),(b) Measured and predicted dimensionless wavenumber spectra during stage II ($h = 0.56$ m for A2, $h = 0.44$ m for A3). Measured wavenumber κ_{meas} is computed from cross-spectral analysis between adjacent wave gauges while κ_{rms} is predicted with Eq. (17); κ_L is the solution to the linear wave dispersion [Eq. (9)]. (c)–(f) The surface elevation energy density spectra $E(\omega)$ of the different linear and nonlinear reconstructions. For both $\zeta_{L,\kappa_{meas}}$ and $\zeta_{L,\kappa_{rms}}$, the dashed lines correspond to the reconstructions without a cutoff frequency at ω_c (vertical gray dashed line at $3.35\omega_p$). The separation between the infragravity and gravity band of frequencies ($0.6\omega_p$) is indicated by the vertical black dashed line. In all panels, the frequency axis is normalized by the peak frequency ω_p, which equals 2.79 Hz for both wave test A2 (left panels) and A3 (right panels).

wave fields (section 5). In contrast with ζ_{L,κ_L}, the linear reconstructions that use measured ($\zeta_{L,\kappa_{meas}}$) or predicted ($\zeta_{L,\kappa_{rms}}$) dominant wavenumbers do not blow up. Discrepancies with ζ_{wg} tend to increase with frequencies but remain small. Around $2\omega_p$, the $\zeta_{L,\kappa_{meas}}$ and $\zeta_{L,\kappa_{rms}}$ reconstructions underpredict the measured spectra, while ζ_{L,κ_L} already slightly overestimates them (see inserts in Figs. 3c,d). Differences between $\zeta_{L,\kappa_{meas}}$ and $\zeta_{L,\kappa_{rms}}$ are marginal and concentrate at frequencies

between $3\omega_p$ and $3.5\omega_p$, where the Boussinesq approximation of κ_{rms} starts diverging from measurements (Figs. 3a,b). Due to noise in the ECM data, a cutoff frequency at $\omega_c = 3.35\omega_p$ was applied for both wave tests. The extension of $\zeta_{L,\kappa_{meas}}$ after ω_c shows that noise in the ECM data only results in a plateau starting around $3.5\omega_p$ (see Figs. 3c,d). This eventually leads to a slight overestimation of energy levels after $5\omega_p$. In contrast, the reconstruction $\zeta_{L,\kappa_{rms}}$ explodes at high frequencies
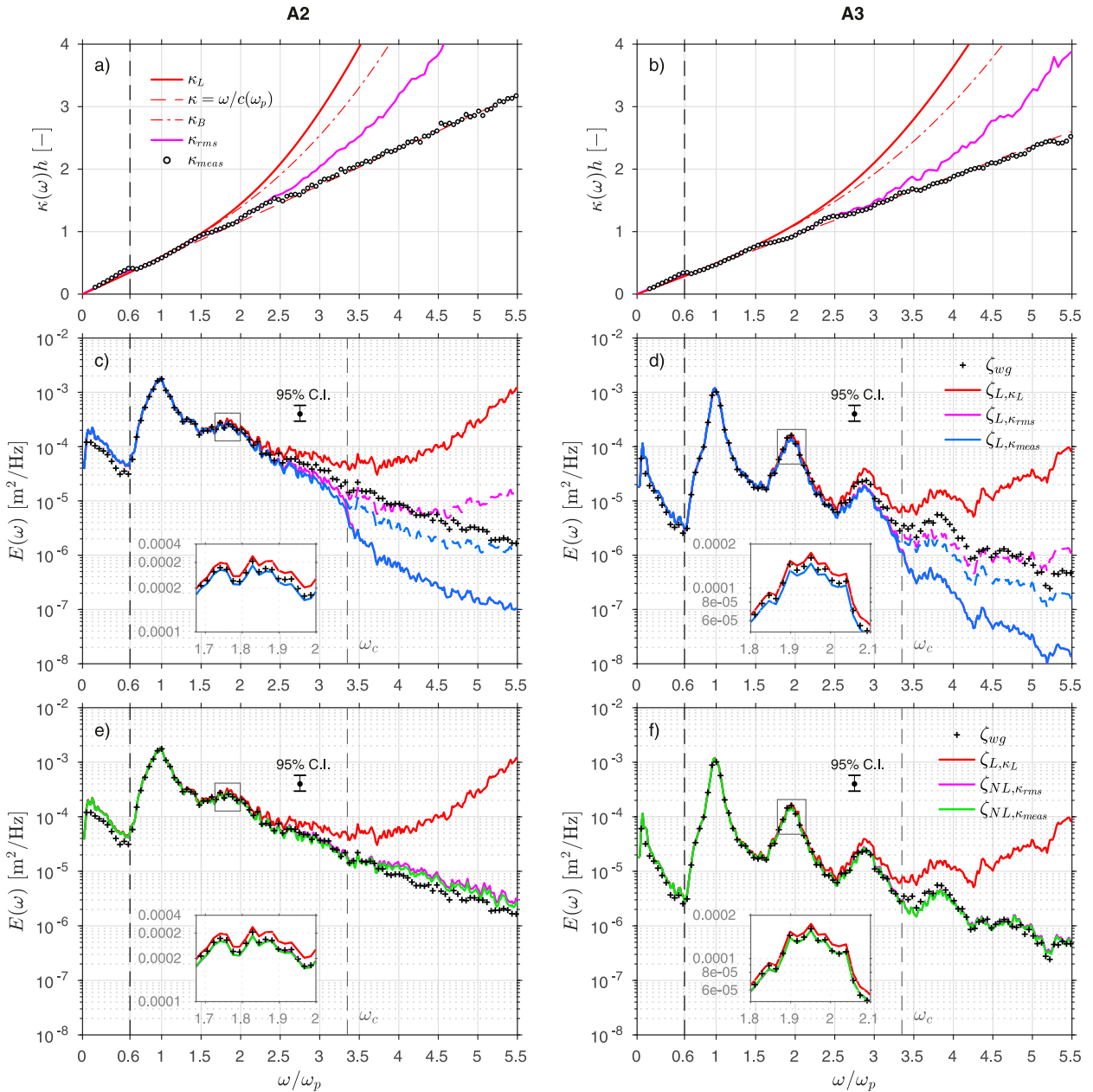
FIG. 4. (a),(b) Measured and predicted dimensionless wavenumber spectra during stage III ($h = 0.41$ m for A2, $h = 0.29$ m for A3). Measured wavenumber κ_{meas} is computed from cross-spectral analysis between adjacent wave gauges while κ_{rms} is predicted with Eq. (17); κ_L is the solution to the linear wave dispersion [Eq. (9)]. (c)–(f) The surface elevation energy density spectra $E(\omega)$ of the different linear and nonlinear reconstructionsy. For both $\zeta_{L,\kappa_{\mathrm{meas}}}$ and $\zeta_{L,\kappa_{\mathrm{rms}}}$, the dashed lines correspond to the reconstructions without a cutoff frequency at ω_c (vertical gray dashed line at $3.35\omega_p$). The separation between the infragravity and gravity band of frequencies ($0.6\omega_p$) is indicated by the vertical black dashed line. In all panels, the frequency axis is normalized by the peak frequency ω_p, which equals 2.79 Hz for both wave test A2 (left panels) and A3 (right panels).

due to the deviations of κ_{rms} from observed dominant wavenumbers at frequencies higher than $3\omega_p$.

For both wave tests, the nonlinear reconstructions $\zeta_{\mathrm{NL},\kappa_{\mathrm{meas}}}$ and $\zeta_{\mathrm{NL},\kappa_{\mathrm{rms}}}$ show excellent skills in estimating energy levels across all frequencies (Figs. 3e,f). Around the second harmonic (see inserts), remarkable improvements are obtained with the nonlinear formula compared to $\zeta_{L,\kappa_{\mathrm{meas}}}$ and $\zeta_{L,\kappa_{\mathrm{rms}}}$. Differences between the two nonlinear reconstructions are very small and concentrate at high

frequencies (e.g., see around $4\omega_p$ for A2). Since the cutoff frequency for the linear reconstructions $\zeta_{L,\kappa_{\mathrm{meas}}}$ and $\zeta_{L,\kappa_{\mathrm{rms}}}$ was here applied at $3.35\omega_p$ (ω_c in Figs. 2–4), energy levels beyond this frequency principally originate from quadratic interactions between components around the peak and the second harmonic (Bonneton and Lannes 2017). For the present case, the inaccuracies of the Boussinesq approximation of Herbers et al. (2002) after $\sim3\omega_p$ hence have little impact on the nonlinear reconstruction. The
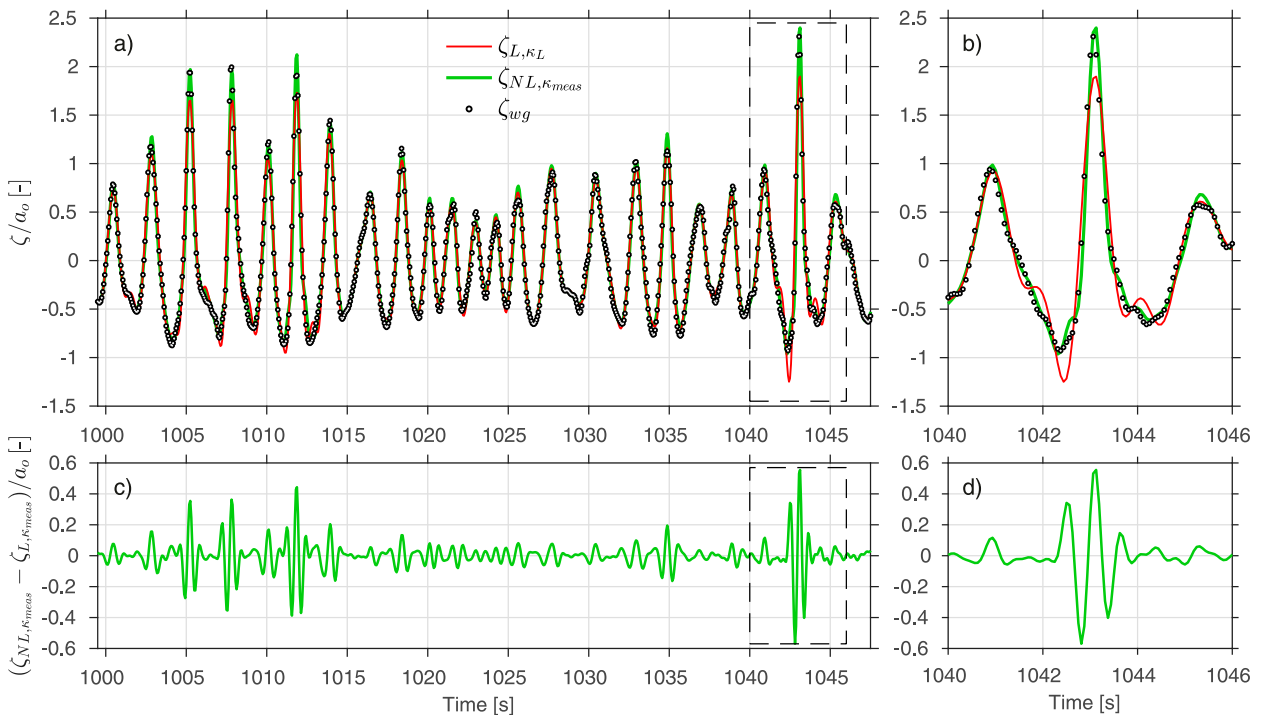
FIG. 5. Comparison of directly measured (ζ_{wg}) and reconstructed (ζ_{L,κ_L} and $\zeta_{NL,\kappa_{rms}}$) surface elevations normalized by the offshore amplitude $a_0 = 0.1$ m at stage II during the wave test A2 ($\kappa_p h = 0.72$, $h = 0.56$ m). (a) A 50-s-long sample and (b) a zoom-in around the extreme wave event occurring around 1042 s (crest elevation $\sim 1.25 H_s$). (c),(d) The contribution of the nonlinear terms to ζ, directly estimated from Eq. (22) as $\zeta_{NL,\kappa_{meas}} - \zeta_{L,\kappa_{meas}}$, and normalized by a_0 are shown below the corresponding panel. A low-pass filter at $2.65\omega_p$ was applied to the linear reconstruction ζ_{L,κ_L} (right before the blow-up, see Fig. 3c).

accuracy of κ_{rms} predictions up to and slightly beyond the second harmonic allow good performances of the reconstruction $\zeta_{NL,\kappa_{rms}}$ at all frequencies (Figs. 3e,f).

b. Shoaling of nonlinear waves in the vicinity of the breaking point (III)

The next regime of propagation (III) considers nonlinear waves approaching the mean breaking point location. Stage III differs from II in two principal aspects: 1) amplitude effects become increasingly important and induce deviations of $O(10\%–15\%)$ between $\kappa(\omega_p)$ and predictions by the linear dispersion relation; 2) the wavenumber and phase velocity spectra become less frequency dependent. As a result, wavenumbers are relatively well described by the simple relation $\omega/c(\omega_p)$ for both tests (Figs. 4a,b). At these depths ($\mu \sim 0.36$ and 0.25 for A2 and A3, respectively), it is worth noting that this relation almost coincides with the shallow-water dispersion relation [Eq. (18)]. The Boussinesq approximation of Herbers et al. (2002) [Eq. (17)] provides very accurate estimates of dominant wavenumbers up to typically $2.5\omega_p$ for A2 and $3\omega_p$ for A3, which is explained by the less dispersive conditions found for A3 at stage III.

Despite the conditions being less dispersive at this stage, the inability of the linear wave dispersion relation to predict wavenumbers at high frequencies still strongly reflects from the energy density spectra of ζ_{L,κ_L} (Figs. 4c,d). Instead of a clear departure as observed in stage II, energy levels

reconstructed with the TFM are observed to flatten between $2.5\omega_p$ and $3.5\omega_p$ and then increase at higher frequencies. As in stage II, the extension of $\zeta_{L,\kappa_{meas}}$ after the cutoff frequency demonstrates that noise in the data is not responsible for the blow-up at high frequencies in intermediate or shallow water depths. Reconstructions (ζ_{L,κ_L} and $\zeta_{L,\kappa_{rms}}$) blow up only when these use wavenumbers that poorly describe the observed dominant dispersive properties of the wave field at high frequencies.

The nonlinear reconstructions $\zeta_{NL,\kappa_{meas}}$ and $\zeta_{NL,\kappa_{rms}}$ correctly reproduce the sea surface spectrum for both wave tests (Figs. 4e,f). While a small overestimation is evidenced for A2 between $4\omega_p$ and $5.5\omega_p$, differences between reconstructed and directly measured surface elevation energy spectra are typically within the 95% confidence interval for A3. Compared to the linear reconstructions, the nonlinear formula [Eq. (6)] substantially improves the description of energy levels at $2\omega_p$ and $3\omega_p$ (see inserts in Fig. 4f in comparison with Fig. 4d), suggesting strong nonlinear effects. Similar to stage II, differences between $\zeta_{NL,\kappa_{meas}}$ and $\zeta_{NL,\kappa_{rms}}$ are marginal, which is again explained by the fact that κ_{rms} values diverge from measurements only after the cutoff frequency ω_c. This is quite a promising result considering that κ_{rms} can be estimated in the field from a single sensor.

c. Wave shape and wave-by-wave statistics

The comparison of $\zeta_{NL,\kappa_{meas}}$ and $\zeta_{NL,\kappa_{rms}}$ spectra with direct measurements attest the capacity of the nonlinear reconstructions

TABLE 4. Surface elevation skewness S_k and mean elevation of the 1/10th largest wave crests $\zeta_{1/10}^c$ computed from the principal reconstructions at stage II ($\kappa_p h = 0.72$ m for A2, $\kappa_p h = 0.63$ m for A3). The relative errors of these parameters are provided between parentheses.

Wave test	A2			A3		
Reconstruction	ζ_{wg}	ζ_{L,κ_L}	$\zeta_{\text{NL},\kappa_{\text{meas}}}$	ζ_{wg}	ζ_{L,κ_L}	$\zeta_{\text{NL},\kappa_{\text{meas}}}$
S_k (—)	0.48 (—)	0.25 (47%)	0.51 (7.9%)	0.52 (—)	0.39 (23.7%)	0.50 (3.6%)
$\zeta_{1/10}^c$ (cm)	15.92 (—)	13.60 (14.6%)	16.57 (4%)	8.98 (—)	8.26 (8.1%)	9.07 (1.1%)

to estimate energy levels at all frequencies. However, such comparisons do not provide information on the wave phase. In the shoaling region, nonlinear wave interactions contribute to the observed surface elevation skewness and play an important role in the occurrence of extreme waves. In this section, we further investigate the ability of the different reconstructions to accurately describe the shape and elevation of individual waves.

Figures 5a and 5b show the reconstructed surface elevations ζ_{L,κ_L} and $\zeta_{\text{NL},\kappa_{\text{meas}}}$ over a sample extracted at stage II during A2 ($\kappa_p h = 0.7$). This example exhibits a moderately energetic group (between 1000 and 1015 s) along with an extreme wave (1040–1045 s, crest elevation $\sim 1.25 H_s$), and a much calmer period in between. The contribution of nonlinear interactions to the reconstructed ζ, which can be directly estimated from Eq. (22) as $\zeta_{\text{NL},\kappa_{\text{meas}}} - \zeta_{L,\kappa_{\text{meas}}}$, is shown in the corresponding bottom panels (Figs. 5c,d). This comparison first shows that the TFM is only suitable during the calm period, when waves are characterized by a low steepness and nonlinear interactions have a weak contribution to ζ (Fig. 5c). When the local amplitude increases, such as during the first wave group or for the extreme wave, ζ_{L,κ_L} consistently underestimates the height and the crest elevation of individual waves. This contrasts with the nonlinear reconstruction $\zeta_{\text{NL},\kappa_{\text{meas}}}$, which systematically improves the description of the height and crest elevation of individual waves. The zoomed region around the largest wave (Fig. 5b) further demonstrates the ability of the nonlinear reconstruction to correctly represent the skewed and peaky shape of extreme waves. Under large-amplitude waves, significant positive and negative contributions from nonlinear interactions are observed (Figs. 5c,d). These contribute positively mostly at the crest level, but also near the surrounding troughs (e.g., Fig. 5b), while they contribute negatively at the front and rear of the wave face. In the case of the extreme wave presented in Fig. 5b, we note that the nonlinear terms explain 25% of the maximal crest elevation. Thus, accounting for nonlinear interactions in the reconstruction problem appears critical in the estimation of wave extrema statistics from subsurface measurements.

These qualitative observations are complemented here with the comparison of two bulk parameters computed from both reconstructed surface elevation time series: the wave skewness S_k (see appendix) and the mean elevation of the 1/10th largest wave crests $\zeta_{1/10}^c$. These two parameters were computed during both wave test and for both stages II (Table 4) and III (Table 5). For the broadband conditions imposed during A2, the underestimation of maximal crests elevation with the TFM is particularly marked in the shoaling region (stage II, Table 4), with a value of $\zeta_{1/10}^c$ that is 15% lower than that computed with ζ_{wg}. This is consistent with the

observations made on Fig. 5. Closer to the breaking point (see Table 5), or for narrowband conditions, this underestimation becomes less significant. The improved predictions of $\zeta_{1/10}^c$ obtained with the nonlinear reconstruction $\zeta_{\text{NL},\kappa_{\text{meas}}}$ further confirm the ability of the reconstruction to describe individual wave statistics ($\zeta_{1/10}^c$ within 4% and 1% during A2 and A3, respectively; see Tables 4 and 5). The qualitative observations made on Fig. 5 about the wave shape are also consistent with the values obtained for the wave skewness S_k. The errors made on this third-order parameter with ζ_{L,κ_L} are within 20%–50% depending on the location and spectral bandwidth imposed (see Tables 4 and 5), while the nonlinear reconstruction $\zeta_{\text{NL},\kappa_{\text{meas}}}$ always predict it within 10%.

The relatively better performances obtained during A3 can be explained by the narrowbanded conditions, which promoted the dominance of forced harmonics at high frequencies. Although both free and forced components can be present, the phase information retained in a Fourier analysis of the subsurface signal per frequency is unique. In the nearshore region, this phase should often be biased toward forced components due to the weaker attenuation expected for forced components across depth compared to free ones. For instance, this could explain the slight overestimation of S_k and $\zeta_{1/10}^c$ at stage II during A2 (Table 4). Nonetheless, the performance of the nonlinear fully dispersive reconstruction is largely sufficient to skillfully estimate wave-by-wave statistics as demonstrated here.

5. Application of the nonlinear fully dispersive reconstruction to field conditions

The previous section demonstrates that when dominant κ spectra of the wave field are known, the sea surface spectrum associated with nonlinear shoaling waves can be accurately estimated at all frequencies with a local application of the nonlinear formula of Eq. (6) in both shallow ($\mu \lesssim 0.3$) and intermediate water depths ($\mu > 0.3$). This is explained by the fact that *temporal* reconstructions that use measured κ spectra (here $\zeta_{L,\kappa_{\text{meas}}}$) are an accurate local approximation of the linear *spatial* reconstruction. In most typical field situations, however, measurements of $\kappa(\omega)$ are not available. The Boussinesq approximation of Herbers et al. (2002) for κ_{rms} [Eq. (17)] remains for now the only possibility to account for nonlinear effects in the dispersive properties of a wave field. In this section, the potential for field applications of the nonlinear moderately[1]

---

[1] As noted earlier, in this case the fully dispersive character of the reconstruction is reduced since the approximation of κ_{rms} is only weakly dispersive; see Table 1.

TABLE 5. Surface elevation skewness S_k and mean elevation of the 1/10the largest wave crests $\zeta^c_{1/10}$ computed from the principal reconstructions at stage III ($\kappa_p h = 0.60$ m for A2, $\kappa_p h = 0.50$ m for A3). The relative errors of these parameters are provided between parentheses.

Wave test	A2			A3		
Reconstruction	ζ_{wg}	ζ_{L,κ_L}	$\zeta_{\mathrm{NL},\kappa_{\mathrm{meas}}}$	ζ_{wg}	ζ_{L,κ_L}	$\zeta_{\mathrm{NL},\kappa_{\mathrm{meas}}}$
S_k (—)	0.75 (—)	0.60 (19.8%)	0.75 (1.8%)	1.05 (—)	0.85 (19%)	0.95 (9.5%)
$\zeta^c_{1/10}$ (cm)	15.22 (—)	14.46 (5%)	15.84 (4%)	11.31 (—)	10.50 (7%)	11.17 (1.2%)

dispersive reconstruction based on κ_{rms} is investigated with the data collected during the Anglet experiments.

The accuracy of κ_{rms} spectral estimates not only depends on the range of validity of the Boussinesq approach employed in Herbers et al. (2002), but also on the nature of the signal used to compute this quantity. In the field, κ_{rms} is typically computed from the pressure signal, since the sea surface elevation is the unknown. Figures 6a and 6b compare κ_{rms} spectral estimates

computed at the deepest location (SIG1) from two different sources: the hydrostatic reconstruction ζ_{hyd} and the directly measured surface elevation ζ_{AST}. The deviations of κ_{rms} from κ_B suggest significant nonlinear effects in the dispersive properties during both events. These effects are strongest for the narrow-band spectra (Fig. 6b), during which forced high harmonics dominate [e.g., see around $2f_p$ where $\kappa_{\mathrm{rms}} \sim \omega/c(\omega_p)$]. The two estimates of κ_{rms} differ by less than 2% at most frequencies for
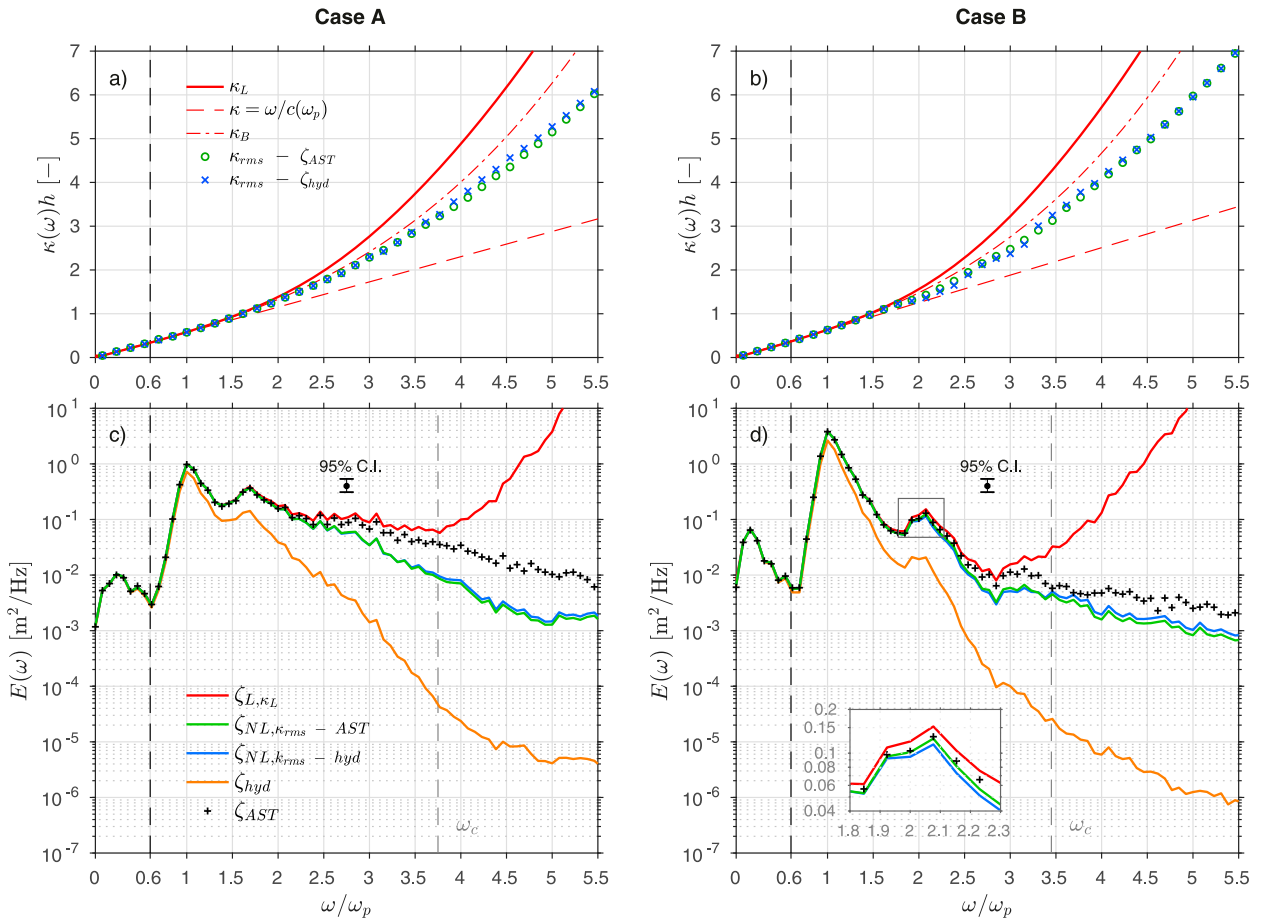

FIG. 6. (a),(b) Dimensionless wavenumber spectra predicted at SIG1 ($h = 13.1$ m for case A, $h = 15.3$ m for case B). κ_{rms} spectra predicted with Eq. (17) are computed from two different sources: ζ_{AST} and ζ_{hyd}. For the sake of readability, only one in two points is shown. (c),(d) Comparison of the energy density spectra of the different reconstructions with those estimated from the directly measured surface elevation ζ_{AST}. The gray vertical dashed lines indicate the cutoff frequency ω_c used for the moderately dispersive linear reconstructions $\zeta_{L,\kappa_{\mathrm{rms}}}$. The separation between the infragravity and gravity band of frequencies ($0.6\omega_p$) is indicated by the black vertical dashed line. In all panels, the frequency axis is normalized by the peak frequency ω_p, which equals 0.48 Hz for both case A (left panels) and B (right panels).
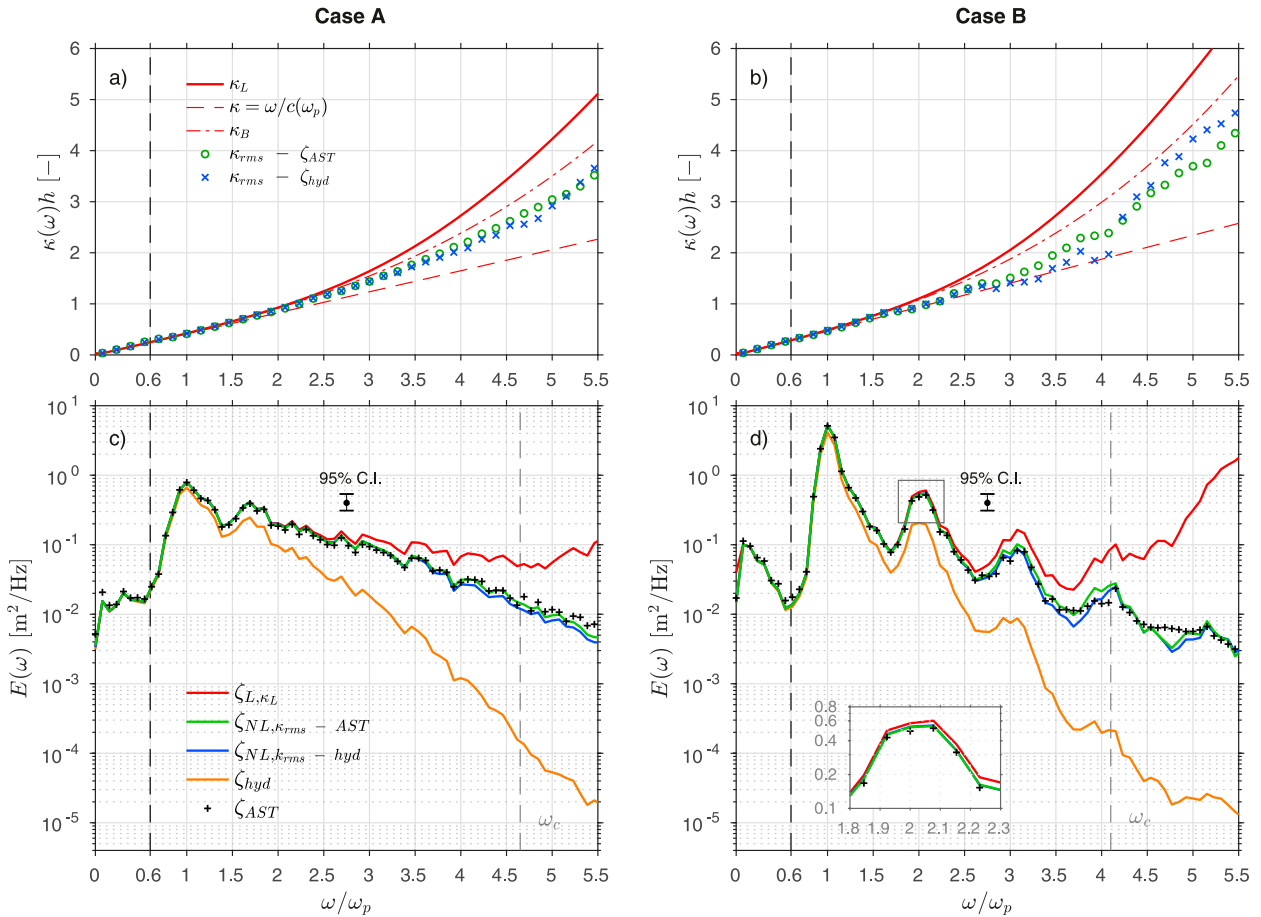
FIG. 7. (a),(b) Dimensionless wavenumber spectra predicted at SIG2 ($h = 7.2$ m for case A, $h = 9.5$ m for case B). κ_{rms} spectra predicted with Eq. (17) are computed from two different sources: ζ_{AST} and ζ_{hyd}. For the sake of readability, only one in two points is shown. (c),(d) Comparison of the energy density spectra of the different reconstructions with those estimated from the directly measured surface elevation ζ_{AST}. The gray vertical dashed lines indicate the cutoff frequency ω_c used for the moderately dispersive linear reconstructions $\zeta_{L,\kappa_{rms}}$. The separation between the infragravity and gravity band of frequencies ($0.6\omega_p$) is indicated by the black vertical dashed line. In all panels, the frequency axis is normalized by the peak frequency ω_p, which equals 0.48 Hz for both case A (left panels) and B (right panels).

case A, with the largest errors (~5%) observed around $4\omega_p$, where predictions of κ_{rms} are less reliable in such water depths. For case B, κ_{rms} values computed from ζ_{hyd} are 8%–15% lower than those computed from ζ_{AST} between $1.5\omega_p$ and $3\omega_p$, which suggests a negative bias due to the dominance of forced components in ζ_{hyd} at these frequencies. As they concentrate at high frequencies, where sea surface energy levels are low, differences in the computations of κ_{rms} have a relatively small impact on the reconstructed signals (Figs. 6c,d).

The performances of the nonlinear reconstructions at SIG1 are quite mixed, with an accurate description of energy levels typically up to $2.5\omega_p$, where the predictions of κ_{rms} are reliable. At higher frequencies, sea surface energy levels are underestimated in both broadband and narrowband cases. In such water depths and wave conditions [$U_r \sim O(0.2)$, see Table 3], the application of Boussinesq theory starts to be questionable. This most likely explains the limitations of the Boussinesq approximations of Herbers et al. (2002) for describing the dispersive properties of the wave field at high frequencies and in particular

the dominance of free components observed at these depths. This is consistent with the smaller underestimations observed for the narrowbanded conditions, which promote the dominance of forced harmonics at high frequencies. For the two energetic cases considered here, the TFM exhibits a very similar behavior as that observed in laboratory conditions: energy levels are overestimated in a region starting around $2\omega_p$ (see insert in Fig. 6d) and up to 3–$3.5\omega_p$, before the reconstructions blow up.

The larger deviations of κ_{rms} from κ_B observed at SIG2 (Figs. 7a,b) compared to those at SIG1 suggest that nonlinear amplitude effects in the dispersive properties of the wave field [β_{am} in Eq. (17)] intensify closer to shore during both events. For the narrowband case B, dominant wavenumbers follow the simple dispersion relation $\omega/c(\omega_p)$, suggesting that the energy at high frequencies is predominantly forced. Similar to the situation at SIG1, κ_{rms} estimates computed from the two sources (ζ_{hyd} and ζ_{AST}) during case A differ by less than 2% except for frequencies larger than $3.5\omega_p$ (maximum difference of ~6%). However, the κ_{rms} spectra computed from ζ_{hyd}
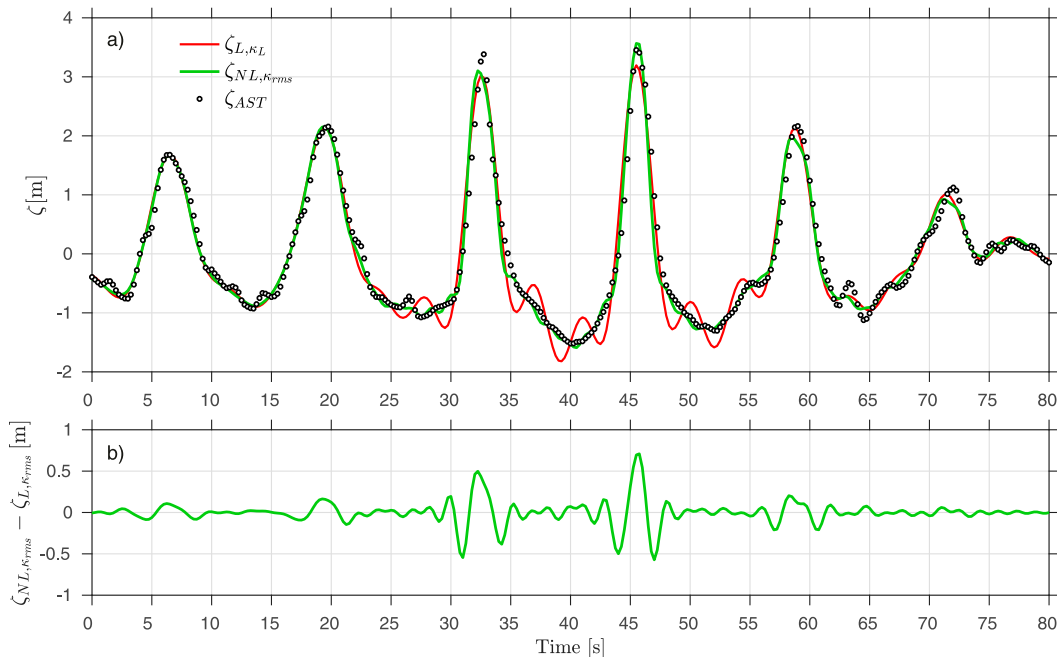
FIG. 8. Example of wave group extracted during case B at SIG2 ($\kappa_p h = 0.49$, $h = 9.5$ m; 1845 local time 13 Oct 2018): (a) the directly measured (ζ_{AST}) and reconstructed (ζ_{L,κ_L} and $\zeta_{NL,\kappa_{rms}}$) surface elevations and (b) the contribution of the nonlinear terms to ζ, directly estimated from Eq. (22) as $\zeta_{NL,\kappa_{rms}} - \zeta_{L,\kappa_{rms}}$. A low-pass filter at $3.5\omega_p$ was applied to the linear reconstruction ζ_{L,κ_L}. Cutting at higher frequencies (e.g., $4\omega_p$ or $4.25\omega_p$) results in even larger unrealistic oscillations at the trough levels. For this comparison, $\zeta_{NL,\kappa_{rms}}$ corresponds to the reconstruction using κ_{rms} values computed from ζ_{AST}.

provide quite unreliable values at frequencies between $2.5\omega_p$ and $4.5\omega_p$ for the narrowbanded wave conditions, likely due to more intense forced components. These estimates can be easily improved with an iterative process: starting from the wavenumber spectra $\kappa_{rms}^{(0)}$ computed from ζ_{hyd}, the wavenumbers $\kappa_{rms}^{(j)}$ at the iteration j can be recomputed from the nonlinear fully dispersive reconstruction of ζ that is based on $\kappa_{rms}^{(j-1)}$. Two iterations are sufficient to reach convergence and decrease the initial mean absolute percentage error of 8% between the two computations of κ_{rms} (ζ_{hyd} and ζ_{AST}, Fig. 7b) to around 3%.

In the Boussinesq regime (Ursell number Ur ~ 0.8), the estimations of κ_{rms} from the AST are highly reliable and explain the excellent performances reached by the nonlinear reconstruction $\zeta_{NL,\kappa_{rms}}$ for both broadband and narrowband events (Figs. 7c,d). For the moderately energetic conditions characterizing both events, the TFM (ζ_{L,κ_L}) leads to strong overestimations of energy levels at relatively high frequencies (one order of magnitude around $4\omega_p$ or $5\omega_p$ depending on the case). Most importantly, these overestimations occur at frequencies below the cutoff frequency that would typically be applied for estimating bulk parameters from this reconstruction: $4.5\omega_p$ (0.35 Hz) and $4\omega_p$ (0.3 Hz) for cases A and B, respectively. The excess of energy in ζ_{L,κ_L} energy spectra up to these frequencies represent an overestimation of the significant wave height H_s by 7% and 5% for cases A and B, respectively, while the mean wave period T_{m02} is underestimated by 11% in both cases. It is worth noting that for optimal choices of cutoff

frequency for ζ_{L,κ_L} (i.e., right before the observed blow-up), an opposite trend for H_s was observed in the surf zone (Martins et al. 2020b), with the surface elevation variance being consistently underestimated with the TFM due to relatively higher levels of energy missed at high frequencies. Since large fractions of the sea surface energy levels at high frequencies originate from interactions between primary components and with their first harmonics, the choice of ω_c has only a weak influence on the computation of bulk parameters from the $\zeta_{NL,\kappa_{rms}}$ reconstructions.

At the wave-by-wave scale, the overestimation of sea surface energy levels by the TFM at relatively high frequencies leads to the appearance of unrealistic oscillations in ζ_{L,κ_L}, regardless of the spectral bandwidth. This is illustrated in Fig. 8 with the example of a wave group measured at SIG2 during case B. On the contrary, the proposed moderately dispersive reconstruction accurately describes the flatter troughs and the sharpness of the highest waves (see the two largest waves of the group in Fig. 8a). Compared to the laboratory setting described in section 4c, the contribution from the nonlinear terms to the reconstructed ζ (Fig. 8b) shows a slightly different behavior. At the trough levels, the contribution from nonlinear terms is weak, which suggests that the spurious oscillations in ζ_{L,κ_L} are mostly explained by the overamplification of high frequency components with the TFM (and to a lesser extent by nonlinear interactions). In contrast, nonlinear interactions contribute positively at the crest level and negatively at the front and rear of the wave
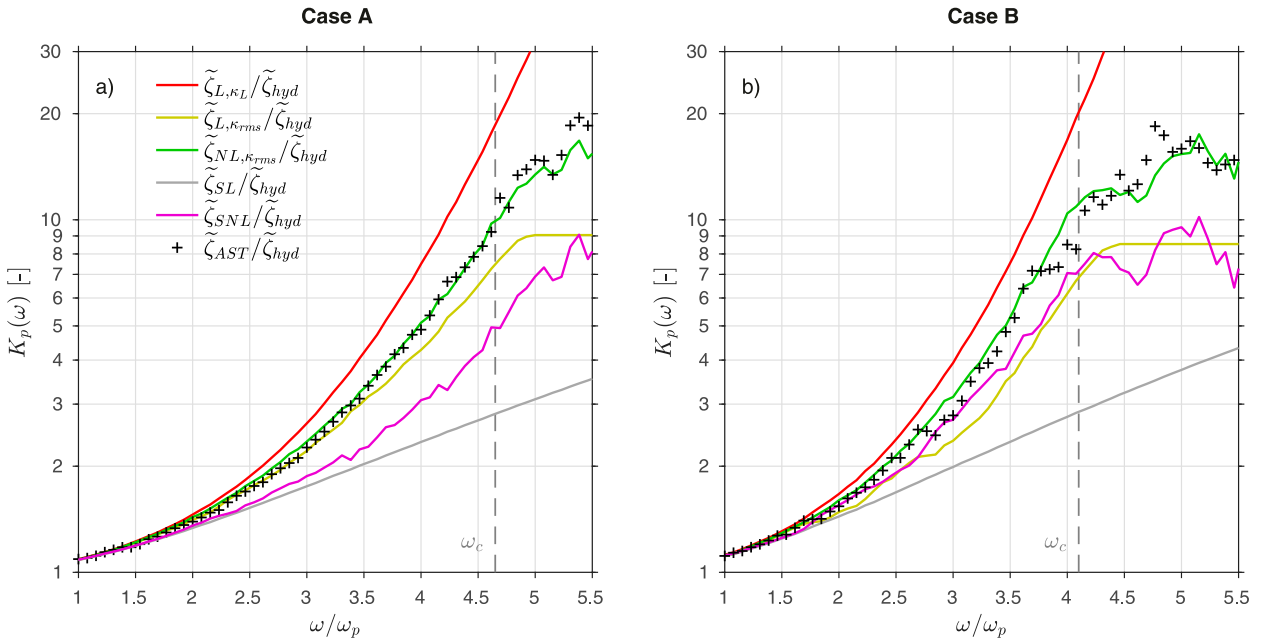
FIG. 9. Transfer functions corresponding to the different linear (ζ_{L,κ_L}, $\zeta_{L,\kappa_{rms}}$, and ζ_{SL}) and nonlinear ($\zeta_{NL,\kappa_{rms}}$ and ζ_{SNL}) reconstructions of ζ for the broadband case A ($\kappa_p h = 0.42$, $h = 7.2$ m) and narrowband case B ($\kappa_p h = 0.49$, $h = 9.5$ m) at SIG2. These are compared with $\tilde{\zeta}_{AST}/\tilde{\zeta}_{hyd}$, which corresponds to the observed transfer function, needed to pass directly from ζ_{hyd} to ζ_{AST}. The gray vertical dashed lines indicate the cutoff frequency ω_c used for the moderately dispersive linear reconstruction $\zeta_{L,\kappa_{rms}}$. In both panels, the frequency axis is normalized by the peak frequency ω_p, which equals 0.48 Hz for both case (a) A and (b) B.

face. Overall, these contributions have for effect to increase the peakiness of the largest waves. As during GLOBEX, this explains why the present approach results in improved estimates of the sea surface skewness in the field (15% error instead of 25% for ζ_{L,κ_L}).

6. On the influence of the spectral bandwidth and directional spreading

By controlling the efficiency of nonlinear energy transfers between triads of frequencies, both the spectral bandwidth and directional spreading are expected to influence nonlinear effects on the dispersion relation of irregular waves (Elgar and Guza 1985b; Herbers et al. 2002, 2003; Martins et al. 2021). Boussinesq model-based predictions by Herbers and Burton (1997) suggest only a weak influence from the directional spreading angle on the efficiency of sum interactions, which are those of interest here. For spreading angles as large as 60°, these authors predict a weaker growth of high-harmonic bound waves by only 10%–20%. More recently, de Wit et al. (2020) noted variations of approximately 10% for smaller directional spreading angles, which are more commonly found in the nearshore region. As during GLOBEX, where unidirectional waves are considered, the differences in dispersive properties observed for cases A and B in Anglet are hence principally explained by the contrasting spectral bandwidth characterizing these events (Herbers et al. 2002; Martins et al. 2021). The influence of the spectral bandwidth on the transfer functions K_p and K_u is here further analyzed using the field data collected

at SIG2, where κ_{rms} estimates are most reliable. In particular, the contrasting wave conditions in terms of spectral bandwidth provide good examples for discussing the application range of the weakly dispersive method of Bonneton et al. (2018) and relate it to the moderately and fully dispersive reconstructions proposed in this study.

Figure 9 examines, for the two contrasting cases A and B, the transfer functions K_p corresponding to the different moderately and weakly dispersive reconstructions investigated here. These are compared with $\tilde{\zeta}_{AST}/\tilde{\zeta}_{hyd}$, which is the observed transfer function, needed to pass from ζ_{hyd} to ζ_{AST}. The overestimation of dominant wavenumbers by the dispersion relation observed in section 5 results in the consistent overestimation of K_p at all frequencies (6%–8% at $2\omega_p$ and up to a factor 2 around $4\omega_p$) for both broadbanded (Fig. 9a) and narrowbanded (Fig. 9b) incident wave conditions. This is consistent with the deviations obtained with the TFM from observed attenuation of u or p across the vertical previously reported in shallow water depths (e.g., see Constantian 1999; Elgar et al. 2001).

For the broadband case A, nonlinear amplitude effects in the dispersion relation [quantified through β_{am}, Eq. (20)] are weak as evidenced by the slight divergence of κ_{rms} from κ_B (Fig. 7a). The transfer function for the linear reconstruction $\zeta_{L,\kappa_{rms}}$ ($\tilde{\zeta}_{L,\kappa_{rms}}/\tilde{\zeta}_{hyd}$) already closely matches the observations and, except at high frequencies, the nonlinear formula only brings marginal improvements (Fig. 9a). When nonlinear amplitude effects are weak, linear wave theory thus provides an accurate estimation of observed K_p as long as accurate κ are
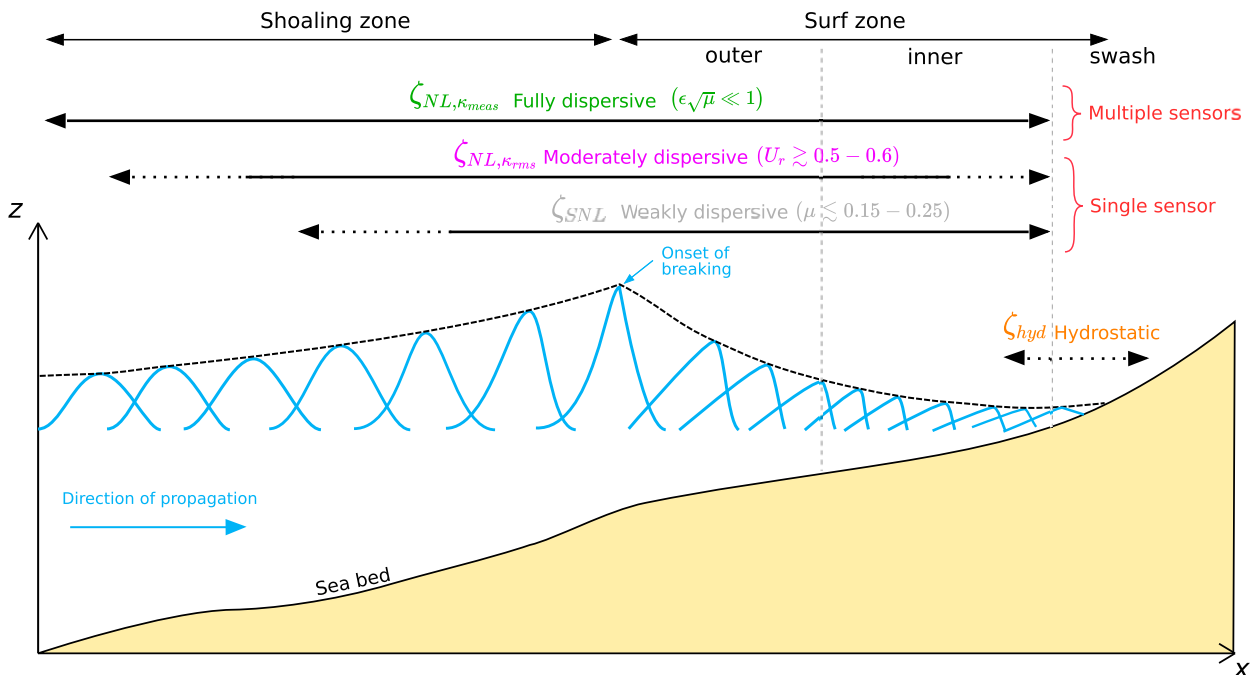
FIG. 10. Synthesis of the temporal reconstruction methods investigated in this study and their range of validity; taken from Mouragues et al. (2019) and updated with the knowledge developed in Martins et al. (2020a,b) and in the present study. The x and z represent the cross-shore and the vertical axes, respectively.

used (here up to $\sim 3.5\omega_p$, see Fig. 9a). Conversely, nonlinear amplitude effects are much stronger for the narrowband case B and balance second-order frequency ones around high harmonics [i.e., $\beta_{\mathrm{fr}} \sim \beta_{\mathrm{am}}$ in Eq. (17)]. As a consequence, most high-frequency components are forced and follow the dispersion relation for nondispersive shallow-water waves [Eq. (18)]. Around $2\omega_p$ and $3\omega_p$, $\tilde{\zeta}_{L,\kappa_{\mathrm{rms}}}/\tilde{\zeta}_{\mathrm{hyd}}$ strongly underestimates the observed transfer function (by $\sim 30\%$) and is much closer to that corresponding to the linear weakly dispersive reconstruction ($\tilde{\zeta}_{\mathrm{SL}}/\tilde{\zeta}_{\mathrm{hyd}}$). The contribution of the nonlinear effects to K_p at these frequencies is much more important than for case A (see contrasting differences between $\tilde{\zeta}_{L,\kappa_{\mathrm{rms}}}/\tilde{\zeta}_{\mathrm{hyd}}$ and $\tilde{\zeta}_{\mathrm{NL},\kappa_{\mathrm{rms}}}/\tilde{\zeta}_{\mathrm{hyd}}$ for both cases in Figs. 9a,b). Through its control on the relative importance of forced energy at high frequencies (Elgar and Guza 1985a; Padilla and Alsina 2017; Martins et al. 2021), the spectral bandwidth is here shown to influence nonlinear effects in the transfer function K_p.

As mentioned in the introduction, the weakly dispersive formula [Eqs. (10) and (11)] are not appropriate when high-frequency components are principally free (i.e., conditions are too dispersive). This is the case here for case A, during which ζ_{SNL} underestimates high-frequency energy levels (Fig. 9a). This occurs even though wave components around the peak frequency approach the shallow water limit ($\mu \sim 0.18$, see Table 3). In contrast, when forced components dominate as during case B ($\mu \sim 0.24$), the linear weakly and fully dispersive reconstructions closely match around $2\omega_p$ and $3\omega_p$ (i.e., $\tilde{\zeta}_{L,\kappa_{\mathrm{rms}}}/\tilde{\zeta}_{\mathrm{hyd}} \sim \tilde{\zeta}_{\mathrm{SL}}/\tilde{\zeta}_{\mathrm{hyd}}$, in Fig. 9b). This explains why both nonlinear reconstructions almost coincide up to $\sim 3.5\omega_p$. The weakly dispersive approach is thus recommendable only when dominant wavenumbers closely match those of

nondispersive shallow-water waves κ_{sw}, i.e., when most wave components travel at the speed of nondispersive shallow-water waves. For broadbanded incident wave spectra, this occurs approximately for $\mu \lesssim 0.1$–0.15, typically close to the mean breaking point location and/or in the surf zone. For narrowbanded incident wave spectra, this can occur in deeper water depths ($\mu \lesssim 0.25$) and covers a region extending from the shoaling zone, where wind seas are negligible compared to forced components, up to the surf zone. For more dispersive conditions, the present nonlinear moderately or fully dispersive approaches need to be employed.

7. Conclusions and perspectives

This study proposes and assesses a nonlinear fully dispersive method for reconstructing the free surface elevation from pressure or wave orbital velocities collected under nonlinear nearshore waves. It relies on the knowledge of dominant wavenumber spectra $\kappa(\omega)$ of the wave field considered in order to account for varying degrees of nonlinearities (i.e., varying amounts of forced energy at a particular frequency). In laboratory conditions, where measurements of $\kappa(\omega)$ are available (κ_{meas}), the nonlinear fully dispersive reconstruction demonstrates excellent skills in diverse nonlinear and dispersive conditions [μ ranging from 0.25 to 0.5, Ur $\sim O(0.1$–1)], and for both broadbanded and narrowbanded incident wave conditions. In the field, where measurements of $\kappa(\omega)$ are rarely available, the reconstruction can use a Boussinesq approximation of κ (κ_{rms}; see Herbers et al. 2002). The accuracy of this moderately dispersive reconstruction is then directly

dependent on that of the Boussinesq approximation for κ_{rms}. Overall, the present results suggest that the relation between p, u and ζ in nearshore nonlinear waves strongly depends on the relative importance of forced components at high frequencies (forced-to-free energy ratio), and our capacity to predict it through, for instance, predictions of κ_{rms}.

Figure 10 synthesizes the range of validity of the different temporal reconstructions investigated in this study. The analysis of field data with contrasting wave conditions in terms of spectral bandwidth clearly illustrates the application range for the weakly dispersive formula of Bonneton et al. (2018). For broad spectra, typically with low fractions of forced energy at high frequencies in intermediate water depths, the application of Eqs. (10) and (11) should be limited to around the breaking point and in the surf zone ($\mu \lesssim 0.15$). In the specific case of narrowbanded incident wave conditions, the application can be extended much farther seaward ($\mu \lesssim 0.25$). The nonlinear fully dispersive approach described herein can be seen as an extension of previous work to intermediate water depths and to a wider range of incident wave conditions. In the field, however, the deployment of several synchronized sensors to robustly estimate κ_{meas} through cross-spectral analysis is not straightforward (e.g., see Herbers et al. 2002) and sometimes impossible simply due to limited experimental resources. As an alternative, the Boussinesq approximation of κ_{rms} (Herbers et al. 2002) can be used locally for estimating the dominant dispersive properties of the wave field considered: here, similar performances as achieved in the laboratory were reached for Ur typically greater than 0.7–0.8. As seen in section 6, both the weakly and moderately dispersive approaches converge in the shallow water limit and provide the same results. In such cases, however, the weakly dispersive formula has the advantage to work in the temporal domain and does not require the computation of bispectra products, which can be challenging to obtain in shallow water depths (e.g., in macrotidal environments).

Although currently limited to Ur $\gtrsim$ 0.5–0.6, the moderately dispersive approach has a great potential for improving our estimates of the sea surface spectrum tail compared to the TFM, which systematically overestimates energy levels at high frequencies (section 5). This has strong implications for the processing of data collected in the nearshore region during storms and extreme events, and also for the accurate estimation of wave shape parameters and wave extrema. A reanalysis of previously collected datasets that employed the TFM to study wave-by-wave statistics in the nearshore is most likely needed and desired. A fully dispersive approximation of κ will be required to improve the performances in conditions characterized by Ur numbers smaller than typically 0.5.

APPENDIX

Computation of First-, Second-, and Third-Order Parameters

The jth moment of the surface elevation energy density spectra is defined as

$$m_j = \int_{0.6f_p}^{5.5f_p} f^j E(f) \, df. \tag{A1}$$

Except for the TFM reconstruction, all moments are here evaluated between $0.6f_p$ and $5.5f_p$, with f_p the discrete peak frequency, so that the reconstruction is assessed in the short-wave frequency band. For ζ_{L,κ_L}, the upper limit of the integral is here optimally taken at the frequency right before the observed blow-up.

The significant wave height is computed as $H_s = 4\sqrt{m_0}$. The mean wave period T_{m02} is defined as

$$T_{m0,2} = \sqrt{\frac{m_0}{m_2}}. \tag{A2}$$

Finally, the wave skewness is computed as

$$S_k = \frac{\overline{(\zeta - \overline{\zeta})^3}}{\overline{(\zeta - \overline{\zeta})^2}^{3/2}}, \tag{A3}$$

where the overbar denotes the time-averaged operator. For consistency with the computation of H_s and T_{m02}, a low-pass filter at $5.5f_p$ is first applied to ζ.

REFERENCES

Aubrey, D. G., and J. H. Trowbridge, 1985: Kinematic and dynamic estimates from electromagnetic current meter data. *J. Geophys. Res.*, **90**, 9137–9146, https://doi.org/10.1029/JC090iC05p09137.

Bishop, C. T., and M. A. Donelan, 1987: Measuring waves with pressure transducers. *Coastal Eng.*, **11**, 309–328, https://doi.org/10.1016/0378-3839(87)90031-7.

Bonneton, P., and D. Lannes, 2017: Recovering water wave elevation from pressure measurements. *J. Fluid Mech.*, **833**, 399–429, https://doi.org/10.1017/jfm.2017.666.

——, ——, K. Martins, and H. Michallet, 2018: A nonlinear weakly dispersive method for recovering the elevation of irrotational

surface waves from pressure measurements. *Coastal Eng.*, **138**, 1–8, https://doi.org/10.1016/j.coastaleng.2018.04.005.

Brodie, K. L., B. Raubenheimer, S. Elgar, R. K. Slocum, and J. E. McNinch, 2015: Lidar and pressure measurements of inner-surfzone waves and setup. *J. Atmos. Oceanic Technol.*, **32**, 1945–1959, https://doi.org/10.1175/JTECH-D-14-00222.1.

Constantian, R. K., 1999: Observed kinematics of waves in the surf zone. M.S. thesis, Dept. of Oceanography, Naval Postgraduate School, 43 pp., https://calhoun.nps.edu/handle/10945/13591.

de Bakker, A. T. M., T. H. C. Herbers, P. B. Smit, M. F. S. Tissier, and B. G. Ruessink, 2015: Nonlinear infragravity-wave interactions on a gently sloping laboratory beach. *J. Phys. Oceanogr.*, **45**, 589–605, https://doi.org/10.1175/JPO-D-14-0186.1.

de Vries, S., D. F. Hill, M. A. de Schipper, and M. J. F. Stive, 2011: Remote sensing of surf zone waves using stereo imaging. *Coastal Eng.*, **58**, 239–250, https://doi.org/10.1016/j.coastaleng.2010.10.004.

de Wit, F., M. Tissier, and A. Reniers, 2020: The relationship between sea-swell bound wave height and wave shape. *J. Mar. Sci. Eng.*, **8**, 643, https://doi.org/10.3390/jmse8090643.

Elgar, S., and R. T. Guza, 1985a: Observations of bispectra of shoaling surface gravity waves. *J. Fluid Mech.*, **161**, 425–448, https://doi.org/10.1017/S0022112085003007.

——, and ——, 1985b: Shoaling gravity waves: Comparisons between field observations, linear theory, and a nonlinear model. *J. Fluid Mech.*, **158**, 47–70, https://doi.org/10.1017/S0022112085002543.

——, E. L. Gallagher, and R. T. Guza, 2001: Nearshore sandbar migration. *J. Geophys. Res.*, **106**, 11 623–11 627, https://doi.org/10.1029/2000JC000389.

Guimarães, P. V., F. Ardhuin, F. Bergamasco, F. Leckler, J.-F. Filipot, J.-S. Shim, V. Dulov, and A. Benetazzo, 2020: A data set of sea surface stereo images to resolve space-time wave fields. *Sci. Data*, **7**, 145, https://doi.org/10.1038/s41597-020-0492-9.

Guza, R. T., and E. B. Thornton, 1980: Local and shoaled comparisons of sea surface elevations, pressures, and velocities. *J. Geophys. Res.*, **85**, 1524–1530, https://doi.org/10.1029/JC085iC03p01524.

Herbers, T. H. C., and M. C. Burton, 1997: Nonlinear shoaling of directionally spread waves on a beach. *J. Geophys. Res.*, **102**, 21 101–21 114, https://doi.org/10.1029/97JC01581.

——, S. Elgar, N. A. Sarap, and R. T. Guza, 2002: Nonlinear dispersion of surface gravity waves in shallow water. *J. Phys. Oceanogr.*, **32**, 1181–1193, https://doi.org/10.1175/1520-0485(2002)032<1181:NDOSGW>2.0.CO;2.

——, M. Orzech, S. Elgar, and R. T. Guza, 2003: Shoaling transformation of wave frequency-directional spectra. *J. Geophys. Res.*, **108**, 3013, https://doi.org/10.1029/2001JC001304.

Kim, Y. C., and E. J. Powers, 1979: Digital bispectral analysis and its applications to nonlinear wave interactions. *IEEE Trans. Plasma Sci.*, **7**, 120–131, https://doi.org/10.1109/TPS.1979.4317207.

Martins, K., C. E. Blenkinsopp, R. Almar, and J. Zang, 2017a: The influence of swash-based reflection on surf zone hydrodynamics: A wave-by-wave approach. *Coastal Eng.*, **122**, 27–43, https://doi.org/10.1016/j.coastaleng.2017.01.006.

——, ——, H. E. Power, B. Bruder, J. A. Puleo, and E. W. J. Bergsma, 2017b: High-resolution monitoring of wave transformation in the surf zone using a LiDAR scanner array. *Coastal Eng.*, **128**, 37–43, https://doi.org/10.1016/j.coastaleng.2017.07.007.

——, P. Bonneton, P. M. Bayle, C. E. Blenkinsopp, A. Mouragues, and H. Michallet, 2020a: Surf zone wave measurements from lidar scanners: Analysis of non-hydrostatic processes. *J. Coastal Res.*, **95**, 1189–1194, https://doi.org/10.2112/SI95-231.1.

——, ——, A. Mouragues, and B. Castelle, 2020b: Non-hydrostatic, non-linear processes in the surf zone. *J. Geophys. Res. Oceans*, **125**, e2019JC015521, https://doi.org/10.1029/2019JC015521.

——, ——, and H. Michallet, 2021: Dispersive characteristics of non-linear waves propagating and breaking over a mildly sloping laboratory beach. *Coastal Eng.*, **167**, 103917, https://doi.org/10.1016/j.coastaleng.2021.103917.

Mouragues, A., P. Bonneton, D. Lannes, B. Castelle, and V. Marieu, 2019: Field data-based evaluation of methods for recovering surface wave elevation from pressure measurements. *Coastal Eng.*, **150**, 147–159, https://doi.org/10.1016/j.coastaleng.2019.04.006.

——, ——, B. Castelle, V. Marieu, R. Jak McCarroll, I. Rodriguez-Padilla, T. Scott, and D. Sous, 2020a: High-energy surf zone currents and headland rips at a geologically constrained mesotidal beach. *J. Geophys. Res. Oceans*, **125**, e2020JC016259, https://doi.org/10.1029/2020JC016259.

——, and Coauthors, 2020b: Field observations of wave-induced headland rips. *J. Coastal Res.*, **95**, 578–582, https://doi.org/10.2112/SI95-113.1.

Padilla, E. M., and J. M. Alsina, 2017: Transfer and dissipation of energy during wave group propagation on a gentle beach slope. *J. Geophys. Res. Oceans*, **122**, 6773–6794, https://doi.org/10.1002/2017JC012703.

Phillips, O. M., 1960: On the dynamics of unsteady gravity waves of finite amplitude. Part 1. The elementary interactions. *J. Fluid Mech.*, **9**, 193–217, https://doi.org/10.1017/S0022112060001043.

Rocha, M. V. L., H. Michallet, and P. A. Silva, 2017: Improving the parameterization of wave nonlinearities – The importance of wave steepness, spectral bandwidth and beach slope. *Coastal Eng.*, **121**, 77–89, https://doi.org/10.1016/j.coastaleng.2016.11.012.

Ruessink, G. B., H. Michallet, P. Bonneton, D. Mouazé, J. L. Lara, P. A. Silva, and P. Wellens, 2013: GLOBEX: Wave dynamics on a gently sloping laboratory beach. *Proc. 7th Int. Conf. on Coastal Dynamics*, Arcachon, France, University of Bordeaux, 1351–1362.

Thornton, E. B., and R. T. Guza, 1982: Energy saturation and phase speeds measured on a natural beach. *J. Geophys. Res.*, **87**, 9499–9508, https://doi.org/10.1029/JC087iC12p09499.

Tissier, M., P. Bonneton, H. Michallet, and B. G. Ruessink, 2015: Infragravity-wave modulation of short-wave celerity in the surf zone. *J. Geophys. Res. Oceans*, **120**, 6799–6814, https://doi.org/10.1002/2015JC010708.